Article

Cell Reports

A Tail-Based Mechanism Drives Nucleosome Demethylation by the LSD2/NPAC Multimeric Complex

Graphical Abstract

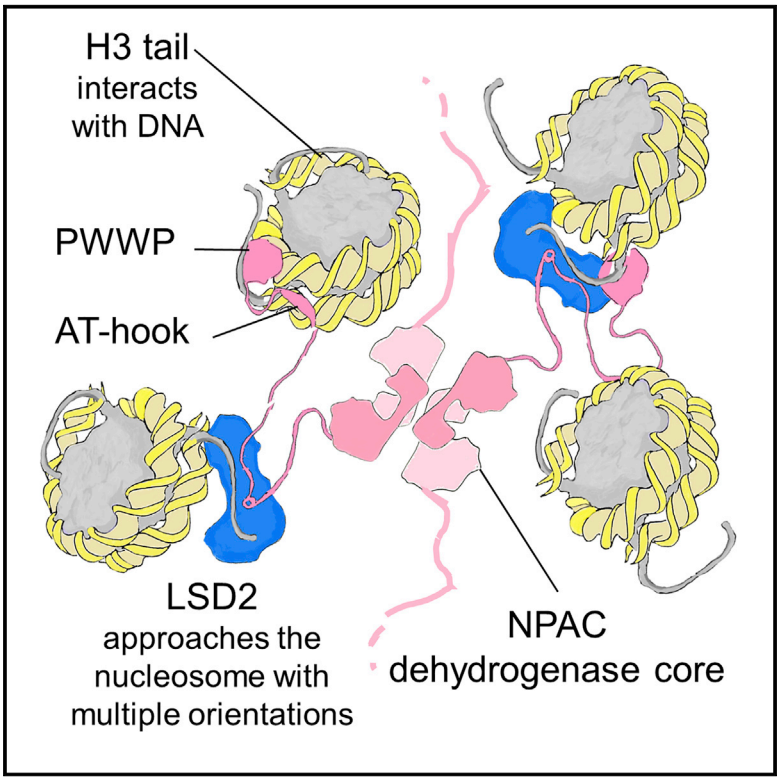

Authors

Chiara Marabelli, Biagina Marrocco, Simona Pilotto, ..., Daniela Rhodes, Sriram Subramaniam, Andrea Mattevi

Correspondence

sriram.subramaniam@ubc.ca (S.S.), andrea.mattevi@unipv.it (A.M.)

In Brief

Through biophysical, biochemical, and structural studies, including cryo-EM, Marabelli et al. describe how NPAC promotes LSD2 productive interaction with the nucleosome in a rapid and flexible manner. Their findings provide a molecular mechanism for LSD2 activity in the context of H3K4me2 demethylation during Pol II transcriptional elongation.

Highlights

- LSD2 demethylase binds nucleosomes by discrete promiscuity at multiple sites
- Nucleosomal DNA represents an intrinsic barrier to histone demethylation
- NPAC has a rigid and catalytically inert oligomerization core and flexible arms
- The NPAC/LSD2 multifunctional enzyme complex modifies transcribed chromatin

Marabelli et al., 2019, Cell Reports *27*, 387–399
April 9, 2019
https://doi.org/10.1016/j.celrep.2019.03.061

CellPress

Cell Reports
Article

A Tail-Based Mechanism Drives Nucleosome Demethylation by the LSD2/NPAC Multimeric Complex

Chiara Marabelli,[1,11] Biagina Marrocco,[1,11] Simona Pilotto,[1,9,11] Sagar Chittori,[2,11] Sarah Picaud,[3] Sara Marchese,[1] Giuseppe Ciossani,[1,10] Federico Forneris,[1] Panagis Filippakopoulos,[3] Guy Schoehn,[4] Daniela Rhodes,[5,6,7] Sriram Subramaniam,[8,*] and Andrea Mattevi[1,12,*]

[1]Department of Biology and Biotechnology "Lazzaro Spallanzani," University of Pavia, via Ferrata 9, 27100 Pavia, Italy
[2]Laboratory of Cell Biology, Center for Cancer Research, National Cancer Institute, NIH, Bethesda, MD 20892, USA
[3]Structural Genomics Consortium, Nuffield Department of Clinical Medicine, University of Oxford, Headington, Oxford OX3 7DQ, UK
[4]Institut de Biologie Structurale (IBS), University Grenoble Alpes, CEA, CNRS, 38044 Grenoble, France
[5]Institute of Structural Biology, Nanyang Technological University, 59 Nanyang Drive, Singapore 636921, Singapore
[6]School of Biological Sciences, Nanyang Technological University, 60 Nanyang Drive, Singapore 637551, Singapore
[7]Lee Kong Chian School of Medicine, Nanyang Technological University, 59 Nanyang Drive, Singapore 636921, Singapore
[8]The University of British Columbia, 2215 Wesbrook Mall, Vancouver, BC V6T 1Z3, Canada
[9]Present address: Darwin Building, University College London, Gower Street, London WC1E 6BT, UK
[10]Present address: Department of Mechanistic Cell Biology, Max Planck Institute of Molecular Physiology, Otto-Hahn-Strasse 11, 44227 Dortmund, Germany
[11]These authors contributed equally
[12]Lead Contact
*Correspondence: sriram.subramaniam@ubc.ca (S.S.), andrea.mattevi@unipv.it (A.M.)
https://doi.org/10.1016/j.celrep.2019.03.061

SUMMARY

LSD1 and LSD2 are homologous histone demethylases with opposite biological outcomes related to chromatin silencing and transcription elongation, respectively. Unlike LSD1, LSD2 nucleosome-demethylase activity relies on a specific linker peptide from the multidomain protein NPAC. We used single-particle cryoelectron microscopy (cryo-EM), in combination with kinetic and mutational analysis, to analyze the mechanisms underlying the function of the human LSD2/NPAC-linker/nucleosome complex. Weak interactions between LSD2 and DNA enable multiple binding modes for the association of the demethylase to the nucleosome. The demethylase thereby captures mono- and dimethyl Lys4 of the H3 tail to afford histone demethylation. Our studies also establish that the dehydrogenase domain of NPAC serves as a catalytically inert oligomerization module. While LSD1/CoREST forms a nucleosome docking platform at silenced gene promoters, LSD2/NPAC is a multifunctional enzyme complex with flexible linkers, tailored for rapid chromatin modification, in conjunction with the advance of the RNA polymerase on actively transcribed genes.

INTRODUCTION

Nucleosomes are the tunable elements of chromatin. Multiple signaling pathways converge to build histone post-transcriptional modification patterns and in turn modulate the dynamics of the nucleosome by either directly affecting nucleosome stability or recruiting specific chromatin remodelers. Nucleosome assembly, disassembly, and modification are carried out by enzymatic subunits embedded within large macromolecular complexes (McGinty and Tan, 2015; Kim et al., 2019; Ricketts et al., 2019; Zhou et al., 2019). The histone demethylases LSD1 and LSD2 represent particularly important examples for exploring fundamental molecular mechanisms underlying these processes. These two enzymes share a highly homologous catalytic domain and employ an identical flavin-dependent reaction mechanism to process the same substrate: mono- and dimethyl Lys4 of histone H3 (H3K4me1 and H3K4me2) (Fang et al., 2013; Forneris et al., 2005; Karytinos et al., 2009; Lee et al., 2005; Shi et al., 2004). Despite their similar catalytic cores, LSD1 and LSD2 feature distinct non-catalytic domains, which form distinguishable binding platforms for different partners and accessory subunits. The elongated tower domain of LSD1 is bound tightly to CoREST (co-repressor of RE1 silencing transcription factor [REST]), which is necessary to grasp the histone tail from DNA (Kim et al., 2015; Pilotto et al., 2015). LSD1/CoREST also forms a bifunctional complex with histone deacetylases (HDAC1 and HDAC2) to establish chromatin repression at gene promoters (Marabelli et al., 2016; Shi et al., 2004). In contrast, LSD2 does not interact with HDACs and CoREST (Chen et al., 2013; Ciccone et al., 2009; Fang et al., 2010, 2013; Nagaoka et al., 2015; Zhang et al., 2013). The biological partner of LSD2 is NPAC (a cytokine-like nuclear factor, also named GLYR1 or NP60), a multidomain protein comprising an N-terminal PWWP domain and a conserved C-terminal dehydrogenase domain (Figure 1A). The two are connected by a long stretch of roughly 170 residues comprising two protein-protein interaction motifs. An AT-hook module (residues 168–180) that binds and activates the mitogen-activated protein kinase (MAPK) p38α is followed by a linker segment (residues 214–225) that binds LSD2 with submicromolar affinity (Figure 1A; Fang et al., 2013; Fu et al., 2006). This short NPAC segment was shown to stimulate the nucleosome-demethylase activity of LSD2 by binding to a

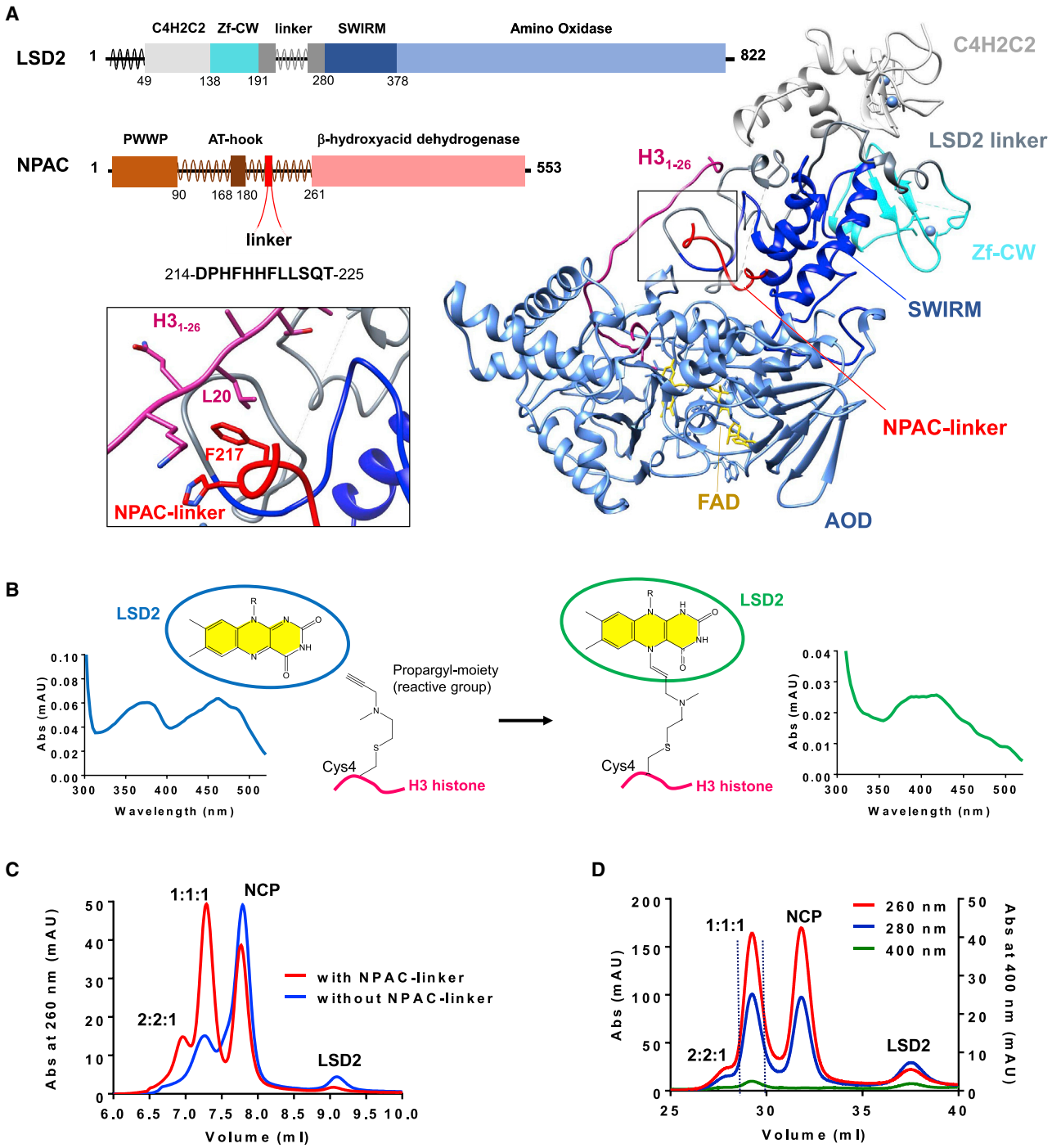

Figure 1. NPAC Linker Sustains Productive Nucleosome Recognition by LSD2

(A) Domain organization of LSD2 and NPAC. Disordered regions are in wavy lines. LSD2 (PDB: 4hsu) is colored according to its multidomain architecture, with the flavin adenine dinucleotide (FAD) in gold and the zinc ions in light blue.

(B) Our semisynthetic nucleosomes form a covalent adduct with the FAD of LSD2 (absorbance peak at 400 nm rather than at 458 nm, as for the oxidized enzyme).

(C) Elution profile (WTC-030S5 column, Wyatt) of semisynthetic NCP (10 μM) and LSD2 (20 μM) after 1 h of incubation with or without the NPAC linker (100 μM). Respectively, 2:2:1 and 1:1:1 stand for $(LSD2/NPAC\text{-}linker)_2$/NCP and LSD2/NPAC-linker/NCP complexes. See also Figure S1.

(D) Elution profile of the LSD2/NPAC-linker/NCP sample used for cryo-EM (dashed lines; three 10/300 columns of Superdex 200 in series, GE Healthcare). Protein, DNA, and the flavin-H3 covalent adduct were detected by monitoring the absorbance at 280, 260, and 400 nm, respectively.

hydrophobic groove between the amine oxidase and the SWIRM domains of the demethylase (Figure 1A; Chen et al., 2013; Fang et al., 2013).

Several studies consistently demonstrate that both LSD2 and NPAC localize within trimethylated Lys36 of histone H3 (H3K36me3)-rich chromatin regions of actively transcribed gene bodies (Fang et al., 2010; Fei et al., 2018; Vermeulen et al., 2010). Depletion of either LSD2 or NPAC leads to similar inhibitory effects on gene transcription elongation (Fang et al., 2010; Fei et al., 2018). This seems to indicate that the LSD2/NPAC system processes chromatin before the passage of the RNA polymerase II (Pol II) elongating complex along DNA. Consistent with this hypothesis, the H3K4me2 signal decreases downstream of Pol II, and it is reconstituted immediately upstream (Barski et al., 2007). However, it remains elusive how a repressive epigenetic signal such as H3K4 demethylation would be important for transcriptional elongation.

The LSD2/NPAC complex represents a canonical example of chromatin regulation by the interplay between catalytic and non-catalytic modules within a single multisubunit nucleosome-modifying complex, but numerous fundamental questions remain to be answered. What is the role of the characteristic non-catalytic domains of LSD2? Do they promote the engagement of the histone tail within the active site? How does the short linker sequence of NPAC stimulate nucleosome demethylation? What is the role of DNA and the histone octamer in substrate recognition? Above all, how do the different architectures of LSD1/CoREST and LSD2/NPAC give rise to their opposing biological outcomes: gene repression by LSD1 versus transcriptional activation by LSD2? Here, we addressed these questions by cryoelectron microscopy (cryo-EM) analysis of the structure and conformational plasticity of the LSD2/nucleosome complex, as well as by dissection of the molecular properties of the multidomain protein NPAC. Our studies lead to the unexpected conclusion that instead of being a nucleosome-docking unit like LSD1/CoREST, LSD2/NPAC is a multimeric enzyme complex exquisitely tailored for the efficient processing of nucleosomal histone tails.

RESULTS AND DISCUSSION

H3K4me1 and H3K4me2 Demethylation Is More Efficient with Longer H3-Tail Peptides but Not Affected by the NPAC Linker

Our first experiments aimed to dissect the binding and kinetics of the human LSD2 demethylase reaction using the recombinant human enzyme expressed in *Pichia pastoris* and several mono- and dimethylated H3 N-terminal peptides (Table 1). First, we confirmed the previously reported faster turnover rates for H3K4me2 over H3K4me1 substrates (Table 1; Chen et al., 2013). Second, we showed that increasing the lengths of the H3 peptides improves LSD2 catalytic efficiency, with as much as an 8-fold lower K_M for the dimethylated 40-residue over the 21-residue substrate. Third, the enzymatic activity was markedly affected by the ionic strength: at 100 mM NaCl, K_M for the $H3_{1–21}$ peptide is 8–10 times higher compared to the value measured in the absence of salt. This effect was less pronounced on the longer $H3_{1–40}$ peptides, for which an increase in K_M was only detectable at 200 mM NaCl (Table 1).

These data indicated that residues 20–40 of the H3 tail feature improved catalytic activity. To investigate their actual contribution to binding, we studied a charge-removing double mutation, targeting two Lys residues in the 21- to 30-residue segment. We found that the K23M-K27M $H3_{1–40}$ peptide is as effective as a substrate as the wild type. Moreover, we tested LSD2 activity at 100 mM NaCl in the presence of 100 μM $H3_{16–40}$ or $H3_{21–40}$ peptides. No inhibition was observed, indicating that the standalone $H3_{16–40}$ and $H3_{21–40}$ segments bind, at best, too weakly to hamper substrate recognition by LSD2 (Table 1). These findings highlight residues 1–20 as the main drivers of H3-tail binding to the demethylase, with the subsequent amino acids enhancing binding, especially under conditions of high ionic strength.

Next, we studied how H3 peptide demethylation is affected and potentially regulated by the NPAC linker (residues 214–225 of NPAC) (Figure 1A; Fang et al., 2013). The outcome of these studies was consistent: the NPAC linker barely influences the steady-state kinetics of H3 peptide binding and demethylation. The only noticeable effect was that NPAC tends to mitigate the worsening (increasing) of peptide K_M values at high NaCl concentrations (150–200 mM) (Table 1).

NPAC Sustains Productive Nucleosome Recognition by LSD2

To focus on the recognition and demethylation mechanisms of the nucleosome, we reconstituted semisynthetic nucleosome core particles (NCPs) with a chemically modified recombinant H3 K4C-C110A double mutant exposing a propargylic group instead of the physiological dimethyl Lys4 side chain (Pilotto et al., 2015). These semisynthetic NCPs function as a suicide substrate: their H3 tail assumes a catalytically competent conformation within the enzyme active pocket and thereby covalently attacks the flavin prosthetic group (Figure 1B). Formation of the covalent NCP/demethylase complex can be easily visualized and quantified by analytical size-exclusion chromatography (Figure 1C).

Incubation trials with LSD2 and the semisynthetic NCPs resulted in poor, albeit clearly detectable, LSD2/NCP complex formation, but the addition of the NPAC-linker peptide led to a marked 7-fold increase in formation of the complex (Figure 1C). This value matches the reported NPAC effect on nucleosome demethylation by LSD2 as measured by published western blot assays (Chen et al., 2013; Fang et al., 2013). We systematically observed the presence of two peaks in the chromatograms. Based on their elution volumes and DNA content, gathered by the relative absorbance at 260 nm, we attributed the major peak to a 1:1:1 LSD2/NPAC-linker/NCP complex and the minor peak to a 2:2:1 complex (i.e., one LSD2/NPAC bound to each H3 of the same NCP). Neither varying the ionic strength nor performing charge-removing mutations of H3 (K23M-K27M) affected nucleosome binding with or without the NPAC linker (Figure S1). Therefore, our semisynthetic NCPs proved to be effective, useful tools for studying nucleosome recognition by LSD2 and the activating role of NPAC.

Table 1. H3K4me1 and H3K4me2 Demethylation Is More Efficient with Longer H3-Tail Peptides but Not Affected by the NPAC Linker

			Monomethyl Lys4[a]		Dimethyl Lys4[a]				
	NPAC[b]	NaCl (mM)	1–21	1–30	1–21	1–30	1–40	1–40 K23M K27M	1–40 + DNA[d]
K_M (μM)	–	0	5.89 ± 0.69	1.34 ± 0.13	1.91 ± 0.18	2.90 ± 0.27	0.99 ± 0.07	0.89 ± 0.05	no activity
	+	0	6.20 ± 0.69	1.18 ± 0.15	2.11 ± 0.19	1.85 ± 0.25	1.09 ± 0.06	0.68 ± 0.08	no activity
	–	50	ND	ND	ND	ND	ND	ND	46.02 ± 7.44
	+	50	ND	ND	ND	ND	ND	ND	>80.00
	–	100	>60.00	5.11 ± 0.79	16.93 ± 3.08	6.18 ± 0.63	2.06 ± 0.25	2.51 ± 0.42	7.00 ± 0.87
	+	100	>60.00	2.36 ± 0.21	16.29 ± 3.59	6.04 ± 0.93	1.55 ± 0.12	1.02 ± 0.11	6.24 ± 0.62
	–	150	ND	ND	ND	13.50 ± 1.54	3.22 ± 0.35	ND	ND
	+	150	ND	ND	ND	8.15 ± 1.11	2.03 ± 0.18	ND	ND
	–	200	ND	ND	ND	ND	6.46 ± 0.58	ND	ND
	+	200	ND	ND	ND	ND	4.94 ± 0.65	ND	ND
k_{cat} (min^{-1})	–	0	0.44 ± 0.01	0.56 ± 0.01	1.01 ± 0.02	1.39 ± 0.03	1.30 ± 0.02	1.24 ± 0.20	no activity
	+	0	0.66 ± 0.02	0.48 ± 0.01	1.02 ± 0.02	1.15 ± 0.04	1.18 ± 0.02	1.04 ± 0.02	no activity
	–	50	ND	ND	ND	ND	ND	ND	1.84 ± 0.15
	+	50	ND	ND	ND	ND	ND	ND	2.42 ± 0.38
	–	100	0.23 ± 0.02	0.41 ± 0.02	0.72 ± 0.05	1.46 ± 0.04	0.83 ± 0.03	0.92 ± 0.04	1.38 ± 0.06
	+	100	0.17 ± 0.03	0.34 ± 0.01	0.70 ± 0.06	1.30 ± 0.07	0.67 ± 0.01	0.64 ± 0.02	1.32 ± 0.04
	–	150	ND	ND	ND	1.01 ± 0.04	1.15 ± 0.03	ND	ND
	+	150	ND	ND	ND	1.19 ± 0.05	1.05 ± 0.02	ND	ND
	–	200	ND	ND	ND	ND	1.23 ± 0.03	ND	ND
	+	200	ND	ND	ND	ND	1.39 ± 0.05	ND	ND
K_d[c] (μM)	–	0	ND	ND	1.99 ± 0.30	ND	ND	ND	ND
	+	0	ND	ND	3.08 ± 0.38	ND	ND	ND	ND

Data are represented as mean ± SEM. All assays were carried out with a peroxidase-coupled method. ND, not determined.

[a]The number of amino acids of the histone H3 N-terminal peptide is indicated.

[b]NPAC-linker sequence 214–225 (Figure 1A).

[c]K_d values were measured by fluorescence polarization using C-terminally tetramethylrhodamine (TAMRA)-labeled histone H3 peptide with sequence ARTKme2QTARKSTGGKAPRKQLA.

[d]The effect of nucleosomal DNA on histone peptide demethylase activity: the 147-bp 601 DNA sequence was used at a final concentration of 0.5 μM.

DNA Interferes with LSD2 Catalysis

Collectively, the experiments with the H3 peptides and the intact nucleosomal particles led to the surprising observations that LSD2 is inhibited by the nucleosome and this inhibition is rescued by the NPAC linker. To investigate the source of this nucleosome-induced inhibitory effect on histone demethylation by LSD2, we first established whether non-substrate histone tails might compete with H3 for the LSD2 active site. We probed the kinetics of peptide demethylation in the presence of high concentrations (100 μM) of $H2A_{1–19}$, $H2A_{117–129}$, $H2B_{4–19}$, or $H4_{1–30}$ peptides. No inhibition was detected, suggesting that the H2A, H2B, and H4 tails do not interfere with LSD2 enzymatic activity (Figure S2). Given this result, we next assayed LSD2 in the presence of the isolated 147-bp 601 Widom DNA to probe its effect on catalysis. At low ionic strength (no NaCl added) activity was hardly detectable in the presence of DNA, both with and without the NPAC linker. The demethylase activity was recovered at 100 mM NaCl, though with a significant 3-fold increase of K_M with respect to the experiments performed in the absence of DNA (Table 1). These findings lead to the fundamental conclusion that a main source of the NCP-exerted inhibition is DNA.

The notion that DNA forms an intrinsic obstacle to nucleosome binding and modification is well documented, and it has been generally ascribed to the pronounced charge density of DNA (McGinty and Tan, 2015; Stützer et al., 2016; Gatchalian et al., 2017; Morrison et al., 2018; Weaver et al., 2018). With reference to LSD2, this phenomenon is functionally crucial, because it is at the heart of the regulatory effect exerted by NPAC. The specific electrostatic interactions between the N-terminal, highly charged, 15 amino acids of H3 and the inner catalytic pocket of the demethylase are inevitably weakened or even compromised by the contiguous crowded-with-charge nucleosomal DNA (Table 1). Conversely, the binding of the $H3_{16–26}$ segment to the outer active-site region of the LSD2/NPAC-linker complex depends less on charged groups (see Table 1 and the K23M-K27M mutation in Figure S1C). Instead, the binding of the $H3_{16–26}$ segment to the LSD2/NPAC-linker complex involves several hydrophobic contacts, especially with Phe217 of NPAC (Figure 1A; Chen et al., 2013; Fang et al., 2013). These interactions are expected to become increasingly more relevant at higher ionic strengths, closer to the physiological conditions, enforcing the influence of NPAC on the LSD2 demethylase activity (Table 1). This NPAC dependency is fully exhibited in the nucleosomal microenvironment, where not only the availability but also conformational flexibility of the tail is limited by the neighboring DNA (Morrison et al., 2018; Weaver et al., 2018).

Single-Particle Cryo-EM Reveals that Multiple Conformations and Few Interactions Characterize the LSD2/NPAC/NCP Complex

To structurally describe the mechanism of nucleosome binding by LSD2/NPAC, we carried out single-particle cryo-EM. We initially employed the semisynthetic nucleosomes reconstituted with the 167-bp 601 Widom sequence that comprises the DNA-linker segments, but the resulting LSD2/NPAC-linker/nucleosome complex could not be separated from the unbound nucleosomes. The semisynthetic NCPs reconstituted with the 147-bp 601 DNA gave excellent chromatographic profiles and enabled the preparative milligram-quantity purification of the covalent LSD2/NPAC-linker/NCP complex (Figure 1D). The specific cross-linking between the LSD2 flavin and the modified H3K4 enabled the purification of an otherwise inherently short-lived enzyme-substrate complex, without the need for external cross-linking agents (Figure 1B). The cryo-EM analysis revealed five distinct structures, and three of them (classes 2–4) correspond to clearly defined LSD2/nucleosome complexes (Figure 2). The demethylase region of the map is always less resolved, suggesting local variability of the LSD2 orientation, but the structures are still fully interpretable (Figures S3 and S4).

In class 2, the body of LSD2 arches over the nucleosome dyad (Figure 2A). The contacts between LSD2 and NCP are confined to two small areas (Figure 3A). In the first one, the H3-tail-binding loop (residues 478–482) of the LSD2 amine oxidase domain contacts the two base pairs of the nucleosomal DNA entry-exit point. In the second contact region, a loop on the C4H2C2 domain of LSD2 (residues 101–107) interacts with a short segment of the H3 α1 helix (around Glu73) and the N-terminal tail of H4 (around Asp24). The trace of the H3 N-terminal segment between the LSD2 catalytic pocket and the nucleosome exit point cannot be revealed at the resolution of our density maps. However, structural analysis predicts that both H3 histones of the NCP can be engaged by LSD2. The first possibility is in line with the LSD2/NPAC-linker/$H3_{1–26}$ co-crystal structure: residues 23–35 of H3 extend over a distance of ~33 Å from the rim of the LSD2 catalytic cleft to the site where the tail protrudes from the nucleosome (dashed in Figure 3A, middle). The second possibility is that Met15 of H3, at the entrance of the LSD2 catalytic pocket, is connected to Lys36, located at the nucleosomal exit point that is closer to LSD2 amine oxidase (35-Å distance) (dashed in Figure 3A, left).

In class 3, the L-shaped LSD2 arches over the edge of the NCP and protrudes laterally from the nucleosomal disk (Figure 2A). The single contact point between the demethylase and the NCP involves a loop on the LSD2 linker region (residues 275–280) and the nucleosomal DNA at the super-helical location (SHL) ± 2 (Figure 3B). The distance covered by H3 from Met15 within the LSD2 active site to Lys36 in the NCP is ~43 Å, which is compatible with multiple extended conformations of the tail (dashed in Figure 3B, right).

From the inspection of the less well-defined class 4 map, it can be inferred that LSD2 sits tangentially to the NCP disk in proximity of the SHL ± 6 (Figure 2A). The putative contact areas on the NCP comprise a few nucleotides, together with residues from H2A (α2 and α3 helices) and H2B (loop α1–α2), close to the acidic patch (Figure 3C).

Despite their strikingly different binding configurations, the LSD2/NPAC-linker/NCP structures share a few insightful features. In all cases, the demethylase-NCP contacts are confined to a few amino acids and nucleotides and there is no extensive interacting surface between the two components. Furthermore, the H3 segment linking the LSD2 active site to the NCP core—from Met15 to Lys36—is always predicted to follow trajectories running along the DNA grooves. Consistently, these trajectories fall within the ensembles of nucleosomal H3-tail conformations

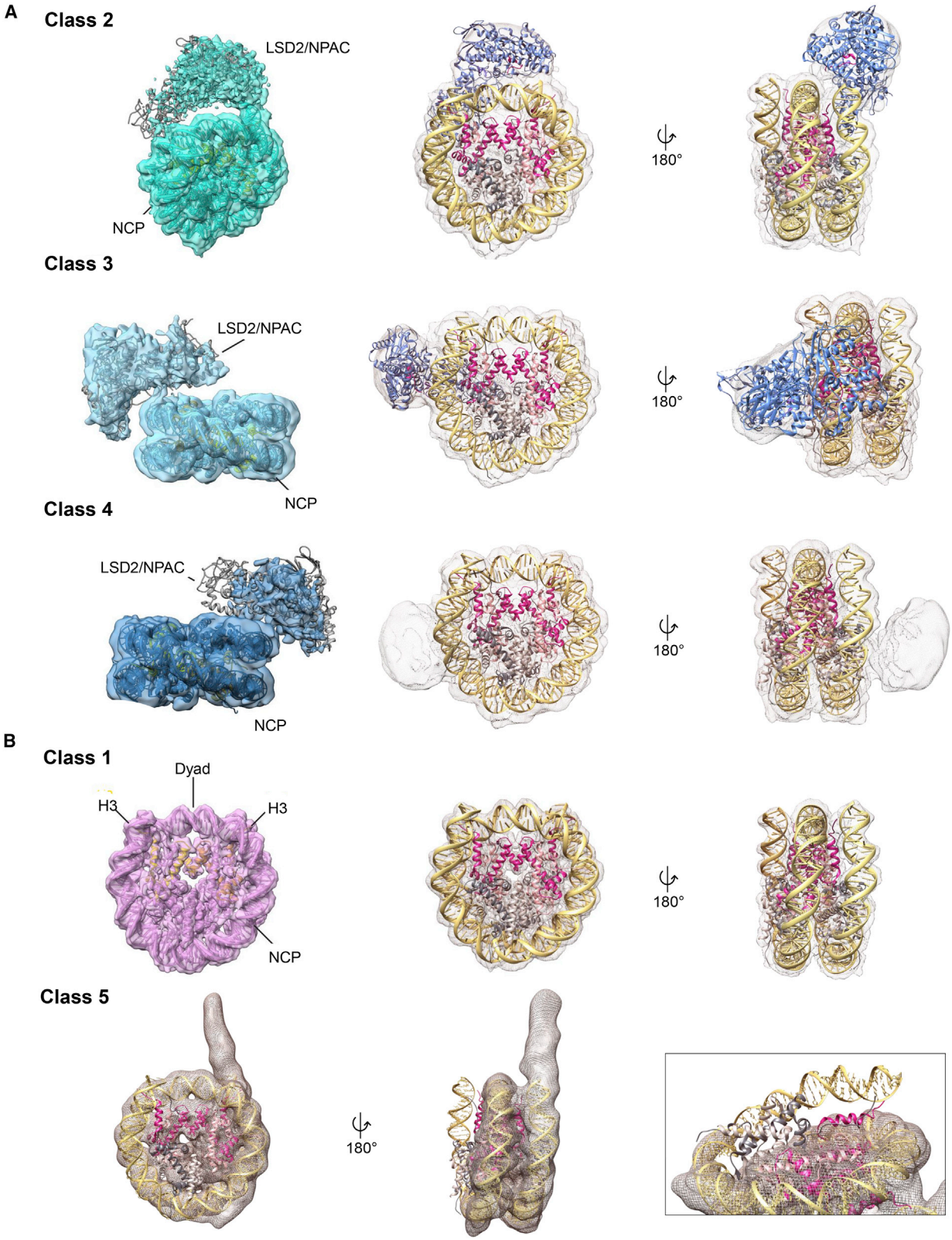

(legend on next page)

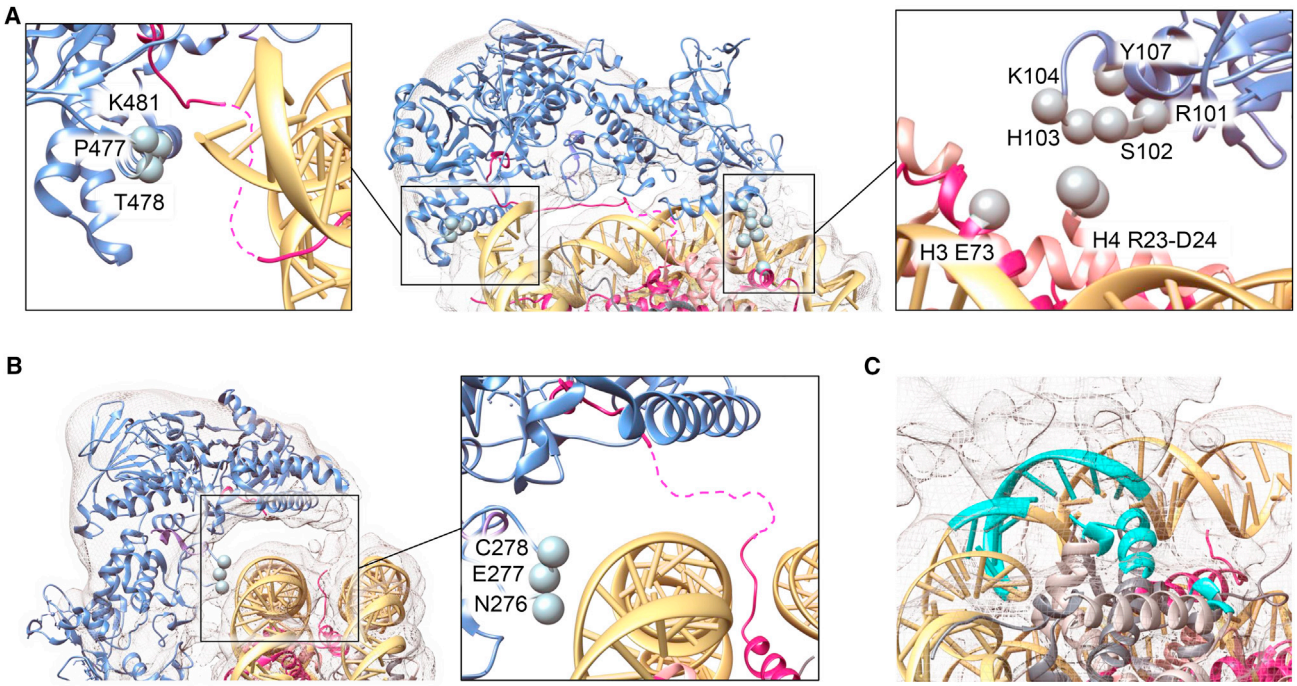

Figure 3. Close-Up Views of LSD2/NCP Interfaces

(A) Class 2 features two contact points between the LSD2 and the nucleosome, depicted in the close-up views.

(B) Class 3 displays a single contact point.

(C) Contact region (in cyan) of class 4 involves DNA super-helical location ± 6 and two short segments of H2A and H2B. Colors are the same as in Figure 2, with the NPAC linker in violet. The density maps are depicted as light gray mesh. Reference residues are labeled, and their Cα atoms are shown as spheres. Dashed lines highlight possible pathways of H3 tails connecting the NCP to the LSD2 catalytic site. See also Figures S3 and S4.

revealed by NMR and computational studies (Morrison et al., 2018). These findings demonstrate that the flexibility of the H3 tail enables multiple and catalytically active binding poses with limited contacts between the LSD2 and the nucleosomal main body.

The cryo-EM analysis revealed two other classes comprising isolated NCPs, though in different states. Class 1 contains roughly half of the particle images and corresponds to the isolated and fully assembled NCP at an overall resolution of 4.02 Å (Figures 2B, S3, and S4). Class 5 represents a hexasome, with its visible protruding DNA. The density map for this class shows that one H2A-H2B dimer is missing and, on the side of the nucleosome where DNA slipped away, the N-terminal α helix of H3 is unfolded (Figures 2C, S3, and S4). The histone-DNA particle featured by class 5 was described previously as a state of nucleosome dynamics and/or unfolding (Bilokapic et al., 2018). Therefore, the same cryo-EM grid allowed us to visualize a partly unfolded NCP, a fully folded particle, and three LSD2 complexes in different conformations.

LSD2 Engages the DNA Template via Electrostatic Interactions

Inspection of the LSD2 protein surface outlines several clusters of positively charged side chains, mostly localized on the zinc-finger domain and in contact with DNA, as shown by the cryo-EM three-dimensional structures (Figures 4A and 4B). To investigate the specificity and magnitude of these interactions, we carried out fluorescence polarization experiments with a 21-bp oligonucleotide. At low ionic strength, full-length LSD2 exhibited nanomolar affinity for DNA, whereas at 100 mM NaCl, the condition used for cryo-EM sample preparation and binding studies, the affinity became barely detectable (Figure 4C; Table S1). To gain more insights into DNA binding by LSD2, we mutated nine Arg and Lys residues that are part of the class 2 and class 3 LSD2/NCP interactions (Figures 4A and 4B), as well as two highly charged disordered segments (the N-terminal 30 residues and the conserved loop 241–258 at the rim of the H3-binding cleft) (Figure 1A). The mutations did not affect DNA binding, with the exception of the N-terminal Δ30 variant, which featured a

Figure 2. Single-Particle Cryo-EM Reveals that Multiple Conformations and Few Interactions Characterize the LSD2/NPAC-Linker/NCP Complex

The quality of the density maps can be best appreciated at the left, whereas model fitting can be best visualized at the right. H2A, H2B, H3, and H4 are shown in dark gray, light gray, purple, and pink, respectively. LSD2 (PDB: 4hsu) is in light blue. The NCP structure used for map fitting was obtained from PDB: 6esf. The DNA molecule is entirely visible in all maps. The first and the last three base pairs were modified to match our 601 sequence exactly. See also Figures S3 and S4.

(A) Overview of the three classes of the LSD2/NPAC-linker/NCP complex. For class 4, LSD2 is tentatively fitted at the left, simply as a reference.

(B) Class 1 represents the intact NCP, whereas class 5 is a partly unfolded NCP: a H2A-H2B dimer is missing, and the N-terminal helix of H3 is unstructured.

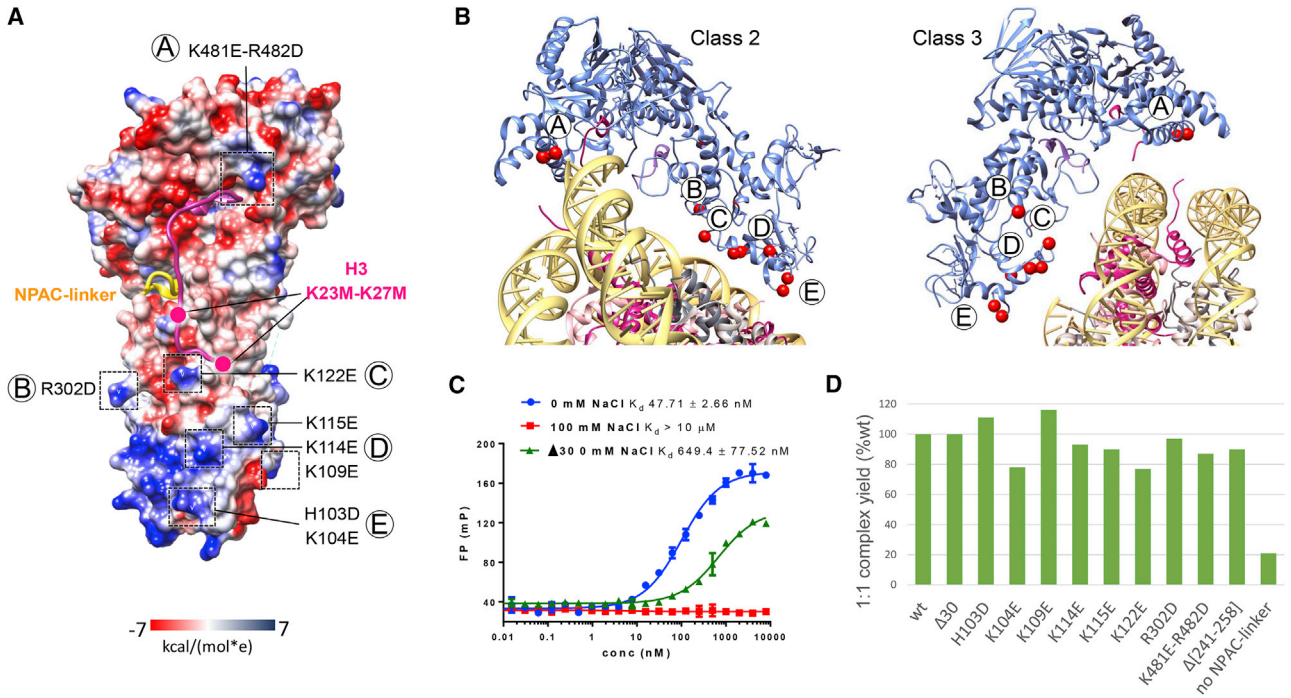

Figure 4. LSD2 Engages the DNA Template via Electrostatic Interactions

(A) The electrostatic surface of LSD2 exposed toward the nucleosome. Positively charged patches characterize the zinc-finger domain and part of the area surrounding the $H3_{1–16}$-binding pocket. The bar indicates the electrostatic potential in kcal/mol*e. Red represents negative electrostatic potential while blue represents positive charge potential.

(B) Close-up views of the LSD2-nucleosome interfaces in class 2 (middle) and class 3 (right), highlighting the LSD2 residues subjected to mutagenesis (red spheres at Cα atoms).

(C) Effect of ionic strength on the binding affinities of full-length and Δ30 LSD2 to DNA. Changes in the fluorescence polarization were measured in millipolarization (mP) units and plotted against LSD2 concentrations. Error bars refer to experiments carried out in triplicate. Data are represented as mean ± SEM. See also Table S1.

(D) Qualitative evaluation of LSD2 mutations on LSD2/NPAC-linker/NCP complex yield. The histogram shows the ratio of the LSD2/NPAC-linker/NCP peak to the absorbance of the free NCP peak (both recorded at 260 nm). The ratios are reported as percentages with reference to LSD2 wild type, which was given the 100% value.

10-fold decrease in affinity (Figure 4C; Table S1). We also found that all mutants bind NCP without drastic alteration in their efficiency with respect to wild-type protein (Figure 4D). These data corroborate the structural findings: LSD2 can weakly bind DNA through salt-sensitive electrostatic interactions. This association is likely brought about by various positively charged patches and does not depend on any specific cluster of residues and/or specific binding geometry.

The PWWP Domain of NPAC Is a H3 Reader and Strongly Binds DNA

In addition to the short LSD2-stimulating linker sequence, NPAC comprises several domains whose molecular functions remain poorly defined (Figure 1A). The NPAC N-terminal PWWP module is homologous to other known H3K36me3 binders (Qin and Min, 2014), in agreement with the NPAC localization at H3K36me3 chromatin loci (Vermeulen et al., 2010). However, NPAC has been shown to bind nucleosomes both with and without specific epigenetic marks (Fei et al., 2018; Sankaran et al., 2016). To determine whether the NPAC PWWP domain is a genuine histone reader, we used the SPOT-peptide array technology, employing a large library of epigenetically modified H3 and H4 peptides (Table S2). We observed a clear selectivity toward peptides containing residues 35–40 of H3, without an evident preference for specific epigenetic markers (Figure S5A). Consistent with this result, isothermal calorimetry performed with the unmodified $H3_{1–40}$ peptide yielded a K_d value of 30 μM (Figure S5B). The unfavorable reduction of conformational entropy upon binding is likely induced by the PWWP-guided partial folding of the 40-residue long peptide, in congruence with the previously characterized PWWP domain-histone peptide interactions (Eidahl et al., 2013; van Nuland et al., 2013). Bio-layer interferometry experiments on $H3_{28–48}$ peptides confirmed the affinity for the H3 C-terminal portion of the H3 tail, with no preference for the methylation states of K36 (Figure S5C). Next, we explored the capability of the NPAC PWWP domain to bind DNA. Fluorescence polarization experiments revealed a strong—primarily electrostatically driven—interaction, described by K_d = 0.68 μM at 100 mM NaCl (Figure S5D). Collectively, these observations highlight the PWWP of NPAC as a potent chromatin binder with very high DNA affinity when compared to other proteins of the same family (van Nuland et al., 2013; Weaver et al.,

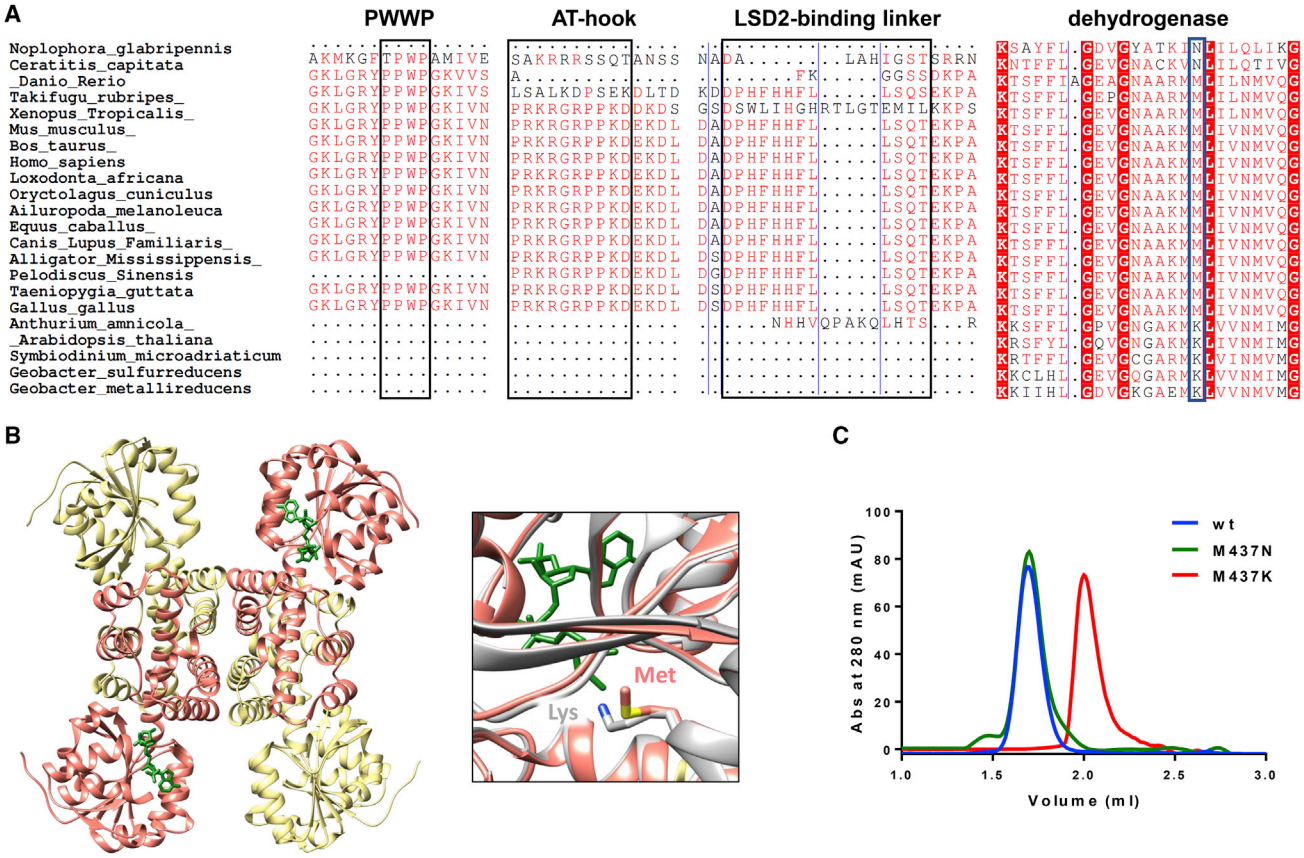

Figure 5. NPAC Dehydrogenase Domain Is Catalytically Impaired and Forms a Stable Tetramer

(A) NPAC homolog sequences are aligned with two representative members of the short-chain alcohol-dehydrogenase family from *Geobacter metallireducens* and *G. sulfurreducens*. The mutation of the catalytic lysine to methionine or asparagine is highlighted within a blue box.

(B) Crystal structure of the NPAC dehydrogenase domain (residues 261–553) shows a tetrameric assembly (PDB: 2uyy). The NADPH is visible in two subunits and is in green. See also Figures S6 and S7 and Table S3. The inset shows the comparison between the active-site regions of the NPAC dehydrogenase (in salmon) and those of the γ-hydroxybutyrate dehydrogenase from *G. sulfurreducens* (PDB: 3pdu; gray).

(C) Elution profiles of wild-type, M437N, and M437K NPAC dehydrogenase domains (5/150 column; Superdex 200, GE Healthcare).

2018; Wen et al., 2014). NPAC has been proposed to function as a nucleosome-destabilizing factor (Fei et al., 2018). Given its tight binding properties, the PWWP is likely responsible for this activity. In the course of our experiments, the nucleosomes tended to extensively precipitate upon mixing with the protein domain, corroborating this hypothesis.

NPAC Dehydrogenase Domain Is a Catalytically Inert, Tetramerization Module

The C-terminal domain of NPAC (residues 261–553) (Figures 1A and 5A) belongs to the highly conserved family of β-hydroxy acid dehydrogenases: cytosolic enzymes catalyzing the NAD^+- or $NADP^+$-dependent oxidation of specific β-hydroxy acid substrates (Njau et al., 2001; Zhang et al., 1999). Sequence homology correlates the dehydrogenase domain of NPAC to glyoxylate reductase. Despite featuring this fascinating topology for a chromatin protein, the function of the NPAC dehydrogenase domain remains unknown. As part of our investigation of the LSD2/NPAC system, we first confirmed that the protein tightly binds nicotinamide adenine dinucleotide phosphate (NADPH; Figure S6). Moreover, gel filtration and small-angle X-ray scattering (SAXS) firmly demonstrated that the protein is tetrameric in solution (Figures 5B and S7; Table S3) (PDB: 2uyy). Therefore, the NPAC dehydrogenase domain is a tetrameric NADH- or NADPH-binding protein that displays features typical of the β-hydroxy acid dehydrogenases.

We observed that the NPAC dehydrogenase domain hosts a methionine residue (Met437) in place of the highly conserved and catalytically essential lysine shared by all β-hydroxy acid dehydrogenase enzymes (Figures 5A and 5B). This finding strongly suggests that NPAC is catalytically inert, at least as a dehydrogenase enzyme. Consistently, a methionine or an asparagine at this position is a conserved feature among all NPAC orthologs exhibiting the LSD2-binding linker sequence (Figure 5A). Along these lines, we characterized two mutants: M437K and M437N. Surprisingly, the M437K protein proved to be monomeric but aggregation prone (Figure 5C) and far less stable than the wild type (10°C lower melting temperature). Conversely, the M437N mutant retained the tetrameric arrangement and, upon addition of NADPH, exhibited a thermostability value comparable to

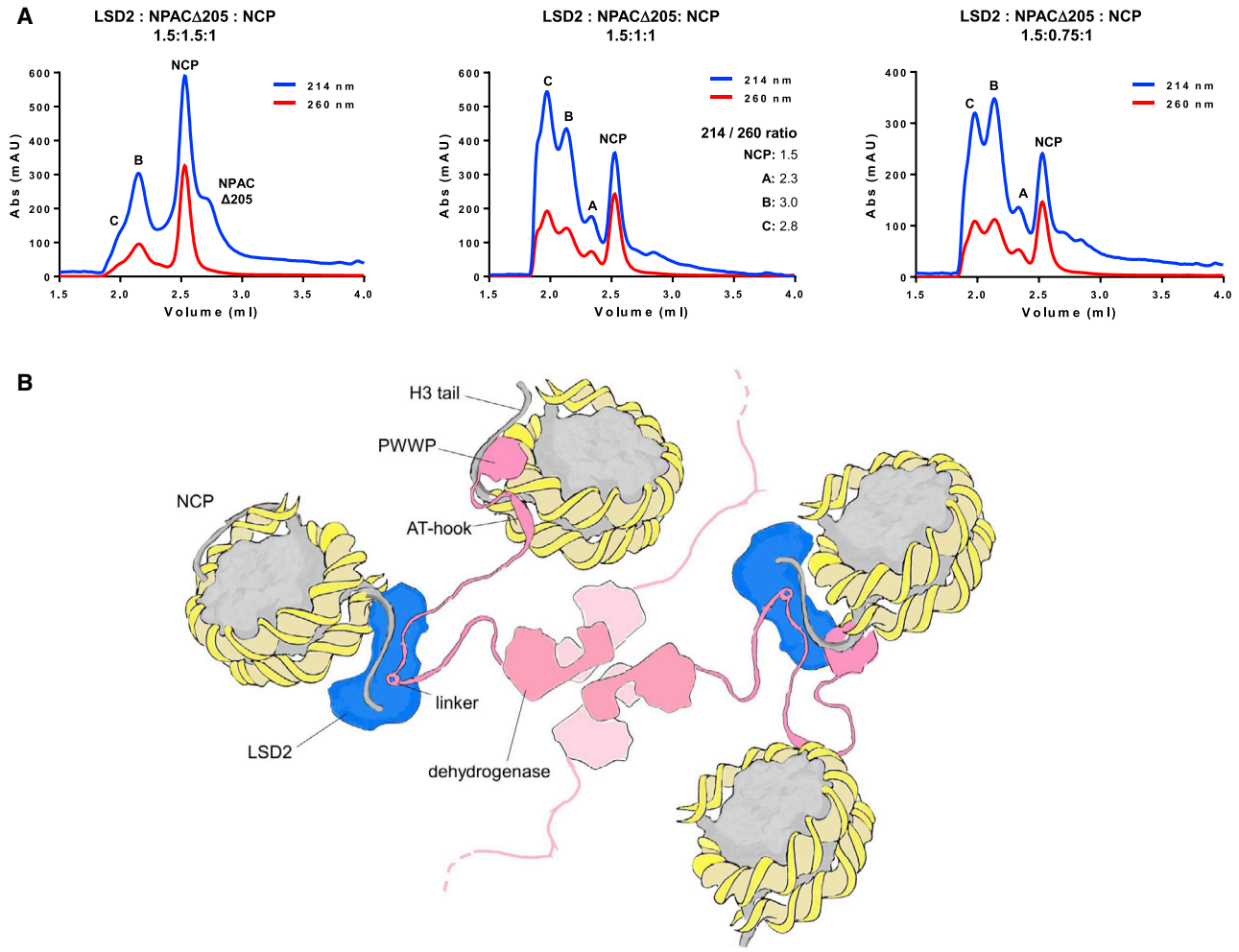

Figure 6. NPAC Tetramer Binds Multiple Copies of LSD2/Nucleosome

(A) NCP, LSD2, and NPACΔ205 (residues 206–553, containing the linker sequence and the dehydrogenase domain; see Figure 1A) were incubated at different molar ratios as shown above each panel (NPACΔ205 concentrations refer to the tetramer, molecular weight [MW] = 151 kDa) (Table S3). Decreasing relative amounts of NPACΔ205 with respect to nucleosome and LSD2 favors the formation of species at a higher molecular weight with greater DNA content (peak C), as calculated from the A_{214}/A_{260} ratio, which reflects the protein/DNA content. Peak A elutes at the same volume of the LSD2/NCP complex containing the NPAC linker only (V_e = 2.35 mL). This peak, occasionally present in the chromatograms, is a species that has lost an intact NPACΔ205 (likely by proteolysis). The experiments were performed on a WTC-030N5 column. See also Figure S7 and Table S3.

(B) Dehydrogenase domain of NPAC forms a stable tetramer decorated by flexible N-terminal arms, which comprise a PWWP domain, an AT-hook region predicted to bind DNA, and the LSD2-activating segment.

that of the wild-type protein. Combining these results, we concluded that in the course of evolution, NPAC lost essential catalytic elements but retained NADH or NADPH binding and consolidated a stable tetrameric assembly. Therefore, the dehydrogenase domain has all features of a stable oligomerization module.

LSD2/NPAC Is a Multimeric Complex

To broaden our understanding of LSD2/NPAC, we designed a human NPAC variant that comprised both the LSD2-binding linker and the C-terminal dehydrogenase domain (NPACΔ205) (Figure 1A). This protein behaved as predicted: it was tetrameric (SAXS data in Figure S7 and Table S3) and retained the ability to bind LSD2 and sustain nucleosome recognition (Figure 6A). These properties enabled the reconstitution of large complexes involving LSD2, tetrameric NPAC, and NCP. With increasing NCP and LSD2 relatively to the NPACΔ205 tetramer, a larger assembly (peak C in the chromatogram of Figure 6A) was favored over a minor yet conspicuous complex species (peak B), which instead prevailed at higher NPACΔ205 concentrations. The peak C complex featured higher DNA content than the peak B species, as indicated by the DNA-to-protein absorbance ratios (A_{214}/A_{260}). The large (~0.5 MDa) size of these complexes was confirmed by SAXS (Figure S7; Table S3). The interpretation of these data is inherently challenging due to the complexity of a system comprising multivalent binding species: the tetrameric NPAC, the dimeric histone core of the nucleosome, and the monomeric LSD2. Nevertheless, the chromatographic profiles,

DNA content analysis, and SAXS data convincingly converge toward the idea that with increasing LSD2 and NCP concentrations, multimeric assemblies form, containing multiple copies of LSD2 and NCP per NPAC tetramer (Table S3).

CONCLUSIONS

The key finding of our work is that LSD2 and NPAC constitute a multimeric system with a rigid core and flexible units. The N-terminal portions of NPAC stretch out from the C-terminal stable tetrameric core, evolved from an ancestral dehydrogenase enzyme. Each of these flexible arms exposes two chromatin-binding modules plus a chromatin-modifying enzyme. The AT hook and the PWWP grasp the nucleosomal particles, possibly increasing the avidity and processivity of neighboring LSD2 enzymes (Figure 6B). The positively charged surface patches featured by LSD2, particularly by the zinc-finger domain, enable its weak association with nucleosomal DNA. Such short-lived encounter complexes drive the formation of the catalytically productive LSD2/NPAC/nucleosome interactions that rely on the NPAC-favored capture of the H3 tail by LSD2. This mode of nucleosome recognition, together with the multimeric architecture of the complex, seems exquisitely suited for processive nucleosome modification, in association with the rapidly advancing RNA polymerase on gene bodies.

It is instructive to compare these mechanistic features with those described for LSD1, the other human flavin-dependent histone demethylase. The overall architecture of LSD1/CoREST is designed to stably clamp the nucleosomes at gene promoters through tight interactions with both the H3 tail and the DNA (Baron and Vellore, 2012; Kim et al., 2015; Pilotto et al., 2015). This nucleosome-docking mode of operation clearly contrasts with the tail-based mechanism of the multimeric and dynamic LSD2/NPAC complex. LSD1 can thereby function to stably induce repression at gene promoters, whereas LSD2 can more dynamically operate to support active gene transcription by the RNA polymerase. Given these contrasting features, it is fascinating that both flavin-dependent systems rely on structurally and mechanistically different auxiliary factors—CoREST and NPAC—to overcome the same inhibitory histone tail-sequestering effect by nucleosomal DNA. Despite their different mechanistic strategies, multidomain architectures of the auxiliary proteins, and opposing biological outcomes, these multiprotein histone demethylase complexes are tailored to license their enzymatic activities only on their appropriate target regions of the chromatin.

STAR★METHODS

Detailed methods are provided in the online version of this paper and include the following:

- KEY RESOURCES TABLE
- CONTACT FOR REAGENT AND RESOURCE SHARING
- EXPERIMENTAL MODEL AND SUBJECT DETAILS
  - Protein expression
- METHOD DETAILS
  - Plasmids cloning and mutagenesis
  - Proteins purification
  - Enzyme activity assays
  - Fluorescence polarization
  - Analytical size-exclusion chromatography
  - Thermal-shift assays
  - HPLC-MS analysis
  - Peptide interaction assay (SPOT blot analysis)
  - Isothermal Titration Calorimetry (ITC)
  - Biolayer Interferometry (BLI)
  - SAXS
  - Cryo-EM sample preparation and data acquisition
  - Image processing
  - Model building and structure analysis
- QUANTIFICATION AND STATISTICAL ANALYSIS
  - Activity assays
  - Fluorescence polarization
  - Thermal-shift assays
  - Domain prediction and sequence alignments
- DATA AND SOFTWARE AVAILABILITY

SUPPLEMENTAL INFORMATION

Supplemental Information can be found online at https://doi.org/10.1016/j.celrep.2019.03.061.

ACKNOWLEDGMENTS

This work was supported by AIRC (IG-11342), MIUR (Flagship Epigen project and PRIN 20152TE5PK), and the Center for Cancer Research at NCI, NIH, Bethesda, MD. The high-resolution datasets were collected at eBIC (Didcot, UK) under proposal em16082 and supported by iNEXT project H2020 (grant 653706) under proposal 2099. The cryo-EM platforms of the Grenoble Instruct Instruct-CERIC Center (ISBG: UMS 3518 CNRS-CEA-UGA-EMBL) are supported by FRISBI (ANR-10-INSB-05-02) and GRAL (ANR-10-LABX-49-01) within the Grenoble Partnership for Structural Biology (PSB) and the Rhône-Alpes Region, the Fondation Recherche Medicale (FRM), the fonds FEDER, and the GIS-Infrastrutures en Biologie Sante et Agronomie (IBISA). We acknowledge eBIC of Diamond Light Source (Didcot, UK) for access to cryo-EM microscopes and all staff members for their essential support and expertise during data collections. This work used the computational resources of the NIH High-Performance Computing (HPC) Biowulf cluster (http://hpc.nih.gov). We acknowledge ESRF (Grenoble, France) for provision of synchrotron radiation facilities and its staff during SAXS data collection. We thank Federica Corana (Centro Grandi Strumenti, Pavia) for support in mass spectrometry, Sergio Valente (Sapienza, University of Rome) for the alkylating reagents, René Bærentsen (Aarhus) for help in mutagenesis, and Sara Sandin (Nanyang Technological University, Singapore) for help in sample optimization and grid preparation. S. Pilotto was recipient of EMBO and EPIGEN short-term fellowships and was awarded with a fellowship from Fondazione Buzzati-Traverso.

AUTHOR CONTRIBUTIONS

All listed authors performed experiments and analyzed data. C.M., B.M., and S. Pilotto performed all biochemical assays. S. Pilotto prepared the cryo-EM samples and collected all datasets. S.S., D.R., F.F., and G.S. supported the cryo-EM experiments. S. Pilotto and S.C. performed image processing. C.M., S. Picaud, and P.F. carried out the experiments with the PWWP domain. S.M. and S. Pilotto performed the experiments on the NPAC dehydrogenase domain. B.M. and F.F. collected and analyzed SEC-SAXS data. C.M., B.M., S. Pilotto, and S.C. prepared figures. All authors contributed to the manuscript.

DECLARATION OF INTERESTS

The authors declare no competing interests.

Received: January 14, 2019
Revised: February 28, 2019
Accepted: March 15, 2019
Published: April 9, 2019

REFERENCES

Barad, B.A., Echols, N., Wang, R.Y.R., Cheng, Y., DiMaio, F., Adams, P.D., and Fraser, J.S. (2015). EMRinger: side chain-directed model and map validation for 3D cryo-electron microscopy. Nat. Methods *12*, 943–946.

Baron, R., and Vellore, N.A. (2012). LSD1/CoREST is an allosteric nanoscale clamp regulated by H3-histone-tail molecular recognition. Proc. Natl. Acad. Sci. USA *109*, 12509–12514.

Barski, A., Cuddapah, S., Cui, K., Roh, T.Y., Schones, D.E., Wang, Z., Wei, G., Chepelev, I., and Zhao, K. (2007). High-resolution profiling of histone methylations in the human genome. Cell *129*, 823–837.

Bateman, A., Martin, M.J., O'Donovan, C., Magrane, M., Alpi, E., Antunes, R., Bely, B., Bingley, M., Bonilla, C., Britto, R., et al.; The UniProt Consortium (2017). UniProt: the universal protein knowledgebase. Nucleic Acids Res. *45* (*D1*), D158–D169.

Bilokapic, S., Strauss, M., and Halic, M. (2018). Histone octamer rearranges to adapt to DNA unwrapping. Nat. Struct. Mol. Biol. *25*, 101–108.

Brennich, M.E., Round, A.R., and Hutin, S. (2017). Online Size-exclusion and Ion-exchange Chromatography on a SAXS Beamline. J. Vis. Exp. *119*, 1–9.

Chen, V.B., Arendall, W.B., 3rd, Headd, J.J., Keedy, D.A., Immormino, R.M., Kapral, G.J., Murray, L.W., Richardson, J.S., and Richardson, D.C. (2010). MolProbity: all-atom structure validation for macromolecular crystallography. Acta Crystallogr. D Biol. Crystallogr. *66*, 12–21.

Chen, F., Yang, H., Dong, Z., Fang, J., Wang, P., Zhu, T., Gong, W., Fang, R., Shi, Y.G., Li, Z., and Xu, Y. (2013). Structural insight into substrate recognition by histone demethylase LSD2/KDM1b. Cell Res. *23*, 306–309.

Ciccone, D.N., Su, H., Hevi, S., Gay, F., Lei, H., Bajko, J., Xu, G., Li, E., and Chen, T. (2009). KDM1B is a histone H3K4 demethylase required to establish maternal genomic imprints. Nature *461*, 415–418.

Dinkel, H., Van Roey, K., Michael, S., Kumar, M., Uyar, B., Altenberg, B., Milchevskaya, V., Schneider, M., Kühn, H., Behrendt, A., et al. (2016). ELM 2016—data update and new functionality of the eukaryotic linear motif resource. Nucleic Acids Res. *44* (*D1*), D294–D300.

Eidahl, J.O., Crowe, B.L., North, J.A., McKee, C.J., Shkriabai, N., Feng, L., Plumb, M., Graham, R.L., Gorelick, R.J., Hess, S., et al. (2013). Structural basis for high-affinity binding of LEDGF PWWP to mononucleosomes. Nucleic Acids Res. *41*, 3924–3936.

Emsley, P., and Cowtan, K. (2004). Coot: model-building tools for molecular graphics. Acta Crystallogr. D Biol. Crystallogr. *60*, 2126–2132.

Fang, R., Barbera, A.J., Xu, Y., Rutenberg, M., Leonor, T., Bi, Q., Lan, F., Mei, P., Yuan, G.C., Lian, C., et al. (2010). Human LSD2/KDM1b/AOF1 regulates gene transcription by modulating intragenic H3K4me2 methylation. Mol. Cell *39*, 222–233.

Fang, R., Chen, F., Dong, Z., Hu, D., Barbera, A.J., Clark, E.A., Fang, J., Yang, Y., Mei, P., Rutenberg, M., et al. (2013). LSD2/KDM1B and its cofactor NPAC/GLYR1 endow a structural and molecular model for regulation of H3K4 demethylation. Mol. Cell *49*, 558–570.

Fei, J., Ishii, H., Hoeksema, M.A., Meitinger, F., Kassavetis, G.A., Glass, C.K., Ren, B., and Kadonaga, J.T. (2018). NDF, a nucleosome-destabilizing factor that facilitates transcription through nucleosomes. Genes Dev. *32*, 682–694.

Filippakopoulos, P., Picaud, S., Mangos, M., Keates, T., Lambert, J.P., Barsyte-Lovejoy, D., Felletar, I., Volkmer, R., Müller, S., Pawson, T., et al. (2012). Histone recognition and large-scale structural analysis of the human bromodomain family. Cell *149*, 214–231.

Forneris, F., Binda, C., Vanoni, M.A., Mattevi, A., and Battaglioli, E. (2005). Histone demethylation catalysed by LSD1 is a flavin-dependent oxidative process. FEBS Lett. *579*, 2203–2207.

Förster, S., Apostol, L., and Bras, W. (2010). Scatter: Software for the analysis of nano-and mesoscale small-angle scattering. J. Appl. Crystallogr. *43*, 639–646.

Franke, D., Petoukhov, M.V., Konarev, P.V., Panjkovich, A., Tuukkanen, A., Mertens, H.D.T., Kikhney, A.G., Hajizadeh, N.R., Franklin, J.M., Jeffries, C.M., and Svergun, D.I. (2017). *ATSAS 2.8*: a comprehensive data analysis suite for small-angle scattering from macromolecular solutions. J. Appl. Crystallogr. *50*, 1212–1225.

Fu, J., Yang, Z., Wei, J., Han, J., and Gu, J. (2006). Nuclear protein NP60 regulates p38 MAPK activity. J. Cell Sci. *119*, 115–123.

Gatchalian, J., Wang, X., Ikebe, J., Cox, K.L., Tencer, A.H., Zhang, Y., Burge, N.L., Di, L., Gibson, M.D., Musselman, C.A., et al. (2017). Accessibility of the histone H3 tail in the nucleosome for binding of paired readers. Nat. Commun. *8*, 1489.

Grant, T., Rohou, A., and Grigorieff, N. (2018). *cis*TEM, user-friendly software for single-particle image processing. eLife *7*, e35383.

Karytinos, A., Forneris, F., Profumo, A., Ciossani, G., Battaglioli, E., Binda, C., and Mattevi, A. (2009). A novel mammalian flavin-dependent histone demethylase. J. Biol. Chem. *284*, 17775–17782.

Kim, S.A., Chatterjee, N., Jennings, M.J., Bartholomew, B., and Tan, S. (2015). Extranucleosomal DNA enhances the activity of the LSD1/CoREST histone demethylase complex. Nucleic Acids Res. *43*, 4868–4880.

Kim, J.A., Kwon, M., and Kim, J. (2019). Allosteric Regulation of Chromatin-Modifying Enzymes. Biochemistry *58*, 15–23.

Konarev, P.V., Volkov, V.V., Sokolova, A.V., Koch, M.H.J., and Svergun, D.I. (2004). PRIMUS: A Windows PC-based system for small-angle scattering data analysis. J. Appl. Crystallogr. *36*, 1277–1282.

Lambert, J.P., Picaud, S., Fujisawa, T., Hou, H., Savitsky, P., Uusküla-Reimand, L., Gupta, G.D., Abdouni, H., Lin, Z.Y., Tucholska, M., et al. (2019). Interactome Rewiring Following Pharmacological Targeting of BET Bromodomains. Mol. Cell *73*, 621–638.e17.

Lee, M.G., Wynder, C., Cooch, N., and Shiekhattar, R. (2005). An essential role for CoREST in nucleosomal histone 3 lysine 4 demethylation. Nature *437*, 432–435.

Li, W., Cowley, A., Uludag, M., Gur, T., McWilliam, H., Squizzato, S., Park, Y.M., Buso, N., and Lopez, R. (2015). The EMBL-EBI bioinformatics web and programmatic tools framework. Nucleic Acids Res. *43* (*W1*), W580–W584.

Lowary, P.T., and Widom, J. (1998). New DNA sequence rules for high affinity binding to histone octamer and sequence-directed nucleosome positioning. J. Mol. Biol. *276*, 19–42.

Lu, A.W., Wang, L., Chen, L., Hui, S., Rabinowitz, J.D., and Rabinowitz, J.D. (2018). Extraction and quantitation of Nicotinamide Adenine Dinucleotide Redox Cofactors. Antioxid. Redox Signal. *28*, 167–179.

Luger, K., Rechsteiner, T.J., Flaus, A.J., Waye, M.M.Y., and Richmond, T.J. (1997). Characterization of nucleosome core particles containing histone proteins made in bacteria. J. Mol. Biol. *272*, 301–311.

Marabelli, C., Marrocco, B., and Mattevi, A. (2016). The growing structural and functional complexity of the LSD1/KDM1A histone demethylase. Curr. Opin. Struct. Biol. *41*, 135–144.

McGinty, R.K., and Tan, S. (2015). Nucleosome structure and function. Chem. Rev. *115*, 2255–2273.

Morrison, E.A., Bowerman, S., Sylvers, K.L., Wereszczynski, J., and Musselman, C.A. (2018). The conformation of the histone H3 tail inhibits association of the BPTF PHD finger with the nucleosome. eLife *7*, e31481.

Nagaoka, K., Hino, S., Sakamoto, A., Anan, K., Takase, R., Umehara, T., Yokoyama, S., Sasaki, Y., and Nakao, M. (2015). Lysine-specific demethylase 2 suppresses lipid influx and metabolism in hepatic cells. Mol. Cell. Biol. *35*, 1068–1080.

Njau, R.K., Herndon, C.A., and Hawes, J.W. (2001). New developments in our understanding of the β-hydroxyacid dehydrogenases. Chem. Biol. Interact. *130–132*, 785–791.

Panjkovich, A., and Svergun, D.I. (2018). CHROMIXS: automatic and interactive analysis of chromatography-coupled small-angle X-ray scattering data. Bioinformatics *34*, 1944–1946.

Pettersen, E.F., Goddard, T.D., Huang, C.C., Couch, G.S., Greenblatt, D.M., Meng, E.C., and Ferrin, T.E. (2004). UCSF Chimera—a visualization system for exploratory research and analysis. J. Comput. Chem. *25*, 1605–1612.

Picaud, S., and Filippakopoulos, P. (2015). SPOTing Acetyl-Lysine Dependent Interactions. Microarrays *3*, 370–388.

Pilotto, S., Speranzini, V., Tortorici, M., Durand, D., Fish, A., Valente, S., Forneris, F., Mai, A., Sixma, T.K., Vachette, P., and Mattevi, A. (2015). Interplay among nucleosomal DNA, histone tails, and corepressor CoREST underlies LSD1-mediated H3 demethylation. Proc. Natl. Acad. Sci. USA *112*, 2752–2757.

Qin, S., and Min, J. (2014). Structure and function of the nucleosome-binding PWWP domain. Trends Biochem. Sci. *39*, 536–547.

Ricketts, M.D., Han, J., Szurgot, M., and Marmorstein, R. (2019). Molecular basis for chromatin assembly and modification by multiprotein complexes. Protein Sci. *28*, 329–343.

Robert, X., and Gouet, P. (2014). Deciphering key features in protein structures with the new ENDscript server. Nucleic Acids Res. *42*, W320–W324.

Rohou, A., and Grigorieff, N. (2015). CTFFIND4: Fast and accurate defocus estimation from electron micrographs. J. Struct. Biol. *192*, 216–221.

Sankaran, S.M., Wilkinson, A.W., Elias, J.E., and Gozani, O. (2016). A PWWP Domain of histone-lysine N-methyltransferase NSD2 binds to dimethylated lys-36 of histone H3 and regulates NSD2 function at chromatin. J. Biol. Chem. *291*, 8465–8474.

Scheres, S.H. (2012). A Bayesian view on cryo-EM structure determination. J. Mol. Biol. *415*, 406–418.

Shi, Y., Lan, F., Matson, C., Mulligan, P., Whetstine, J.R., Cole, P.A., Casero, R.A., and Shi, Y. (2004). Histone demethylation mediated by the nuclear amine oxidase homolog LSD1. Cell *119*, 941–953.

Stützer, A., Liokatis, S., Kiesel, A., Schwarzer, D., Sprangers, R., Söding, J., Selenko, P., and Fischle, W. (2016). Modulations of DNA Contacts by Linker Histones and Post-translational Modifications Determine the Mobility and Modifiability of Nucleosomal H3 Tails. Mol. Cell *61*, 247–259.

van Nuland, R., van Schaik, F.M.A., Simonis, M., van Heesch, S., Cuppen, E., Boelens, R., Timmers, H.M., and van Ingen, H. (2013). Nucleosomal DNA binding drives the recognition of H3K36-methylated nucleosomes by the PSIP1-PWWP domain. Epigenetics Chromatin *6*, 12.

Vermeulen, M., Eberl, H.C., Matarese, F., Marks, H., Denissov, S., Butter, F., Lee, K.K., Olsen, J.V., Hyman, A.A., Stunnenberg, H.G., and Mann, M. (2010). Quantitative interaction proteomics and genome-wide profiling of epigenetic histone marks and their readers. Cell *142*, 967–980.

Weaver, T.M., Morrison, E.A., and Musselman, C.A. (2018). Reading More than Histones: The Prevalence of Nucleic Acid Binding among Reader Domains. Molecules *23*, E2614.

Wen, H., Li, Y., Xi, Y., Jiang, S., Stratton, S., Peng, D., Tanaka, K., Ren, Y., Xia, Z., Wu, J., et al. (2014). ZMYND11 links histone H3.3K36me3 to transcription elongation and tumour suppression. Nature *508*, 263–268.

Zhang, L., Chooback, L., and Cook, P.F. (1999). Lysine 183 is the general base in the 6-phosphogluconate dehydrogenase-catalyzed reaction. Biochemistry *38*, 11231–11238.

Zhang, Q., Qi, S., Xu, M., Yu, L., Tao, Y., Deng, Z., Wu, W., Li, J., Chen, Z., and Wong, J. (2013). Structure-function analysis reveals a novel mechanism for regulation of histone demethylase LSD2/AOF1/KDM1b. Cell Res. *23*, 225–241.

Zheng, S.Q., Palovcak, E., Armache, J.P., Verba, K.A., Cheng, Y., and Agard, D.A. (2017). MotionCor2: anisotropic correction of beam-induced motion for improved cryo-electron microscopy. Nat. Methods *14*, 331–332.

Zhou, K., Gaullier, G., and Luger, K. (2019). Nucleosome structure and dynamics are coming of age. Nat. Struct. Mol. Biol. *26*, 3–13.

Zivanov, J., Nakane, T., Forsberg, B.O., Kimanius, D., Hagen, W.J., Lindahl, E., and Scheres, S.H. (2018). New tools for automated high-resolution cryo-EM structure determination in RELION-3. eLife *7*, e42166.

STAR★METHODS

KEY RESOURCES TABLE

REAGENT or RESOURCE	SOURCE	IDENTIFIER
Bacterial and Virus Strains		
P. Pastoris KM71-H	Invitrogen (ThermoFisher)	Cat#C18200
BL21(DE3)RPplus	Novagen (Merck)	EMD_BIO-69450
BL21(DE3)pLysS	Invitrogen	Cat#C606003
Chemicals, Peptides, and Recombinant Proteins		
Fusion High-Fidelity PCR Master Mix	Invitrogen (Thermo Scientific)	Cat#F531S
In-Fusion HD Cloning Kit	Takara (Clontech)	Cat#638920
1-methyl-1-(prop-2-ynyl)aziridinium chloride	Pilotto et al., 2015	https://www.pnas.org/content/pnas/suppl/2015/02/10/1419468112.DCSupplemental/pnas.1419468112.sapp.pdf
Methanol	Panreac AppliChem	A3493,1000PE
Sodium phosphate monobasic dihydrate	Sigma-Aldrich	CAS: 13472-35-0
Sodium Chloride	Carlo Erba	A194090050
Glycerol	Merck	CAS: 56-81-5
Imidazole	Panreac AppliChem	A1378,0250
Deoxyribonuclease I from bovine pancreas	Sigma-Aldrich	CAS: 9003-98-9
PMSF	Sigma-Aldrich	CAS: 329-98-6
Zirconia beads	BioSpec	Cat. No. 11079107
Miracloth filter paper	Merck	475855
Tris	Panreac AppliChem	A3992,0250
Tris(2-carboxyethyl)phosphine hydrochloride	Sigma-Aldrich	CAS: 51805-45-9
Isopropyl-β-D-thiogalactoside	Sigma-Aldrich	CAS:367-93-1
HEPES	Sigma-Aldrich	CAS: 7365-45-9
Dithiothreitol	Sigma-Aldrich	CAS: 3483-12-3
Peroxidase from horseradish	Sigma Aldrich	CAS:9003-99-0; Cat#P6782
Peptides used in binding and enzymatic assays	China Peptides	http://www.chinapeptides.com/english/index.aspx
Ampliflu Red	Sigma Aldrich	CAS:119171-73-2; Cat#90101
SYPRO Orange	Invitrogen	Cat#S5692
H3 peptide used in ITC	TUFTS	http://tucf.tufts.edu/home/peptide_synthesis
Critical Commercial Assays		
SPOT-blot peptide interaction assay	Picaud and Filippakopoulos, 2015	10.3390/microarrays4030370
Whatman Chromatography paper Grade 1CHR	GE Healthcare Life Sciences	Cat#3001-878
Horseradish peroxidase-conjugated anti-His antibody	Novagen (Merck)	Cat#71841
Pierce ECL Western Blotting Substrate	Thermo Fisher Scientific	Cat#32106
SuperStreptavidin (SSA) Dip and Read Biosensors for kinetic	Forte´Bio	Cat#18-0011
Deposited Data		
147 bp 601 nucleosome (class1)	This paper	EMDataResource: EMD-4704
		PDB: 6R1T
LSD2/NPAC-linker (214-225)/nucleosome (class 2)	This paper	EMDataResource: EMD-4705
		PDB: 6R1U
LSD2/NPAC-linker (214-225)/nucleosome (class 3)	This paper	EMDataResource: EMD-4710
		PDB: 6R25

(*Continued on next page*)

Continued

REAGENT or RESOURCE	SOURCE	IDENTIFIER
LSD2/NPAC-linker (214-225)/nucleosome (class 4)	This paper	EMDataResource: EMD-4711
147 bp 601 nucleosome (class 5)	This paper	EMDataResource: EMD-4712
LSD2/NPAC-linker (214-225)/H3 (1-26)	Fang et al., 2013	PDB: 4HSU
cytokine-like nuclear factor NPAC dehydrogenase (261-553)	http://www.rcsb.org	PDB: 2UYY
LSD2 Δ30 (31-822)	This paper	SASBDB: SASDFU3
nucleosome	This paper	SASBDB: SASDFX3
NPAC dehydrogenase (261-553)	This paper	SASBDB: SASDFV3
NPAC Δ205 (206-553)	This paper	SASBDB: SASDFW3
LSD2 Δ30 (31-822)/NPAC Δ205 (206-553)/ nucleosome	This paper	SASBDB: SASDFY3
Oligonucleotides		
TAMRA labeled 21-nt DNA	Microsynth AG	https://www.microsynth.ch/standard-synthesis.html
Recombinant DNA		
LSD2 and NPAC full-length human genes	GeneArt	https://www.thermofisher.com/us/en/home/life-science/cloning/gene-synthesis/gene-strings-dna-fragments.html
pJ902Express vector	DNA 2.0 (now ATUM)	https://www.atum.bio/catalog/expression-vectors/yeast#CytoplasmicExpression2
NPAC 261-553 in pNIC28-Bsa4 vector	SGC	https://www.thesgc.org/
Software and Algorithms		
Clustal Omega (EMBL-EBI)	Li et al., 2015	https://www.ebi.ac.uk/Tools/msa/clustalo/
ESPript 3	Robert and Gouet, 2014	http://espript.ibcp.fr/ESPript/ESPript/
ELM	Dinkel et al., 2016	http://elm.eu.org/
Uniprot	Bateman et al., 2017	https://www.uniprot.org/
GraphPad Prismversion 6.00 for Windows	GraphPad	https://www.graphpad.com/
MicroCal Origin	Origin	https://www.originlab.com/
Forte´Bio analysis software V.9.0.014	Forte´Bio	www.fortebio.com
CHROMIX	Panjkovich and Svergun, 2018	https://www.embl-hamburg.de/biosaxs/chromixs.html
ATSAS package	Franke et al., 2017	https://www.embl-hamburg.de/biosaxs/software.html
Scatter	Förster et al., 2010	http://www.bioisis.net/tutorial/9
PRIMUS	Konarev et al., 2004	https://www.embl-hamburg.de/biosaxs/primus.html
cisTEM	Grant et al., 2018	https://cistem.org/
MotionCor2	Zheng et al., 2017	http://msg.ucsf.edu/em/software/motioncor2.html
Ctffind	Rohou and Grigorieff, 2015	http://grigoriefflab.janelia.org/ctf
RELION	Scheres, 2012	https://www3.mrc-lmb.cam.ac.uk/relion/index.php?title=Main_Page
Coot	Emsley and Cowtan, 2004	http://www2.mrc-lmb.cam.ac.uk/Personal/pemsley/coot/
Chimera	Pettersen et al., 2004	https://www.cgl.ucsf.edu/chimera/
Other		
Carbon grids for cryo-EM	Quantifoil	https://www.emsdiasum.com/microscopy/products/grids/quantifoil.aspx

CONTACT FOR REAGENT AND RESOURCE SHARING

Further information and requests for resources and reagents should be directed to and will be fulfilled by the Lead Contact, Andrea Mattevi (andrea.mattevi@unipv.it).

EXPERIMENTAL MODEL AND SUBJECT DETAILS

Protein expression

All histone proteins were expressed in BL21(DE3) *pLysS E.coli* cells according to established protocols (Luger et al., 1997). LSD2 full-length proteins were expressed in *E. coli* BL21(DE3). Cells were grown in LB medium supplemented with 100 μg/ml ampicillin under shaking conditions till $O.D._{600nm}$ = 0.8. Induction was performed with 0.5 mM IPTG and 0.1 mM $ZnSO_4$ at 17°C for 18 hours. Cells were collected by centrifugation at 5000 rpm for 10 minutes and stored at −20°C. LSD2Δ30-expressing *P. pastoris* cells were grown in flasks at 30°C under shaking conditions for 72 hours and induced with methanol for 48 hours. Cells were then collected by centrifugation at 4000 rpm for 10 minutes and stored at −20°C. The PWWP domain (residues 1-105) was expressed in *E. coli* BL21(DE3). Cells were grown in 2xYT medium supplemented with 100 μg/ml kanamycin and 1% (w/v) glucose at 37°C until $O.D._{600}$ reached 1. Induction was performed with 0.1 mM IPTG for 16 h at 17°C. NPACΔ205 (linker + dehydrogenase) was expressed in *E. coli* BL21(DE3) RPplus, and cells were induced by autoinducing protocol. Cells were collected by centrifugation at 5000 rpm for 10 minutes and stored at −20°C. NPAC dehydrogenase proteins were expressed in *E. coli* BL21(DE3) RPplus. Cells were grown in TB medium at 37°C under shaking conditions till an $O.D._{600nm}$ of 0.8. Induction was performed with 0.5 mM IPTG at 17°C overnight. Cells were collected by centrifugation at 5000 rpm for 10 minutes and stored at −20°C.

METHOD DETAILS

Plasmids cloning and mutagenesis

All cloning and mutagenesis reactions were performed combining the Phusion High-Fidelity PCR Master Mix (Thermo Scientific) with the In-Fusion HD Cloning Kit (Clontech) protocols. DNA sequences were derived from the 601 Widom sequence (Lowary and Widom, 1998). A pMA vector containing 15 copies of the 147 bp 601 Widom sequence was purchased from GeneArt. DNAs were amplified in *E. coli* DH5α, purified and used for nucleosome reconstitution (Luger et al., 1997). The pET3 vectors (Ampicillin resistance) containing the sequences of the four *Xenopus laevis* histone proteins, were a kind gift from Dr. Toshiya Senda (Biomedicinal Information research Center, National Institute of Industrial Science and Technology, Tokyo). H3 K4C-K23M-K27M-C110A was obtained by two consecutive mutagenesis reactions starting from the H3 K4C-C110A already available in house. The sequence coding for human LSD2Δ30 (residues 31-822) was cloned from the full-length human gene (purchased from GeneArt) into a pJ902Express vector (DNA 2.0) with a C-terminal eGFP-His_8 tag fused to a cleavable Prescission-protease cleavage site. The vector was linearized with PmeI and inserted in the *P. pastoris* KM71-H strain (Invitrogen) genome through electroporation. The sequence coding for the full-length human LSD2 was cloned in a pGEX-6P-1 vector with a GST N-terminal tag fused to a cleavable Prescission-protease cleavage site. All LSD2 mutants were obtained from full length sequence (Figure 4). The gene for human NPAC was purchased from GeneArt and cloned in pET24a, bearing an N-terminal Flag-His_8-SUMO tag followed by Prescission protease recognition site. NPACΔ205 (residues 205-553) and NPAC-PWWP (residues 1-105) were obtained from the full-length construct. The pNIC28-Bsa4 vector carrying the N-terminal His_6 tagged NPAC dehydrogenase (residues 261-553) was a kind gift from Structural Genomics Consortium (SGC) of the University of Oxford (UK).

Proteins purification

All purifications were carried out at 4°C, except for the histones, DNA sequences, and NPAC dehydrogenase performed at 20°C. Chromatographic steps were performed on ÄKTA systems (GE Healthcare).

Recombinant nucleosomes were prepared according to established protocols (Luger et al., 1997). H3 mutants K4C-C110A and K4C-K23M-K27M-C110A were alkylated with 1-methyl-1-(prop-2-ynyl)aziridinium chloride as previously described (Pilotto et al., 2015).

LSD2Δ30-expressing *P. pastoris* cells were re-suspended in 50 mM NaH_2PO_4 pH 8.0, 300 mM NaCl, 5% (v/v) glycerol, 25 mM imidazole, 2 μg/ml DNase, and 1 mM PMSF. Zirconia beads (BioSpec products) were used to lyse the cell in a bead-beater. Then beads were removed with a Miracloth filter paper (Merck) and the cell extract was centrifuged at 70,000 g for 30 min. The supernatant was loaded onto a His-Trap column (GE Healthcare). After a wash with 40 mM imidazole, the elution was obtained with 250 mM imidazole. The sample was supplemented with Prescission protease and dialyzed overnight in the same lysis buffer without imidazole. The day after a second His-Trap column step was used to purify the tag-free protein at 40 mM imidazole. The sample was then gel filtered through a Superdex 200 10/300 (GE Healthcare) equilibrated in 20 mM Tris pH 8 (25°C), 100 mM NaCl, 1 mM TCEP.

LSD2 expressing *E. coli* BL21(DE3) cell pellets were re-suspended in 50 mM NaH_2PO_4 pH 8.0, 300 mM NaCl, 5% (v/v) glycerol, 25 mM imidazole, 2% (w/v) lysozyme, and 1 mM PMSF. Cell suspension was sonicated and centrifuged at 70,000 g for 30 min. The supernatant was loaded onto a GST-Trap column (GE Healthcare) and the tagged-protein eluted with 50 mM GSH. His-Prescission protease was added (1 mg/15 mL of sample). The sample was dialyzed overnight in 50 mM NaH_2PO_4 pH 8.0, 300 mM NaCl and

5% glycerol. After dialysis, the sample was loaded onto a second GST-Trap to remove the GST-tag. The unbound fractions were then loaded onto a His-Trap column to remove the His-tagged protease. A final size-exclusion chromatography step was performed on a Superdex 200 10/300 equilibrated in 20 mM Tris pH 8 (25°C), 200 mM NaCl, 1 mM TCEP.

The PWWP domain (residues 1-105) expressing cells were resuspended in 50 mM NaH_2PO_4 pH 8.0, 300 mM NaCl, 5% (v/v) glycerol, 1 mM PMSF and sonicated. The suspension was centrifuged at 56,000 g for 1 h and the cell extract was loaded onto a His-Trap column. The resin was washed first with 50 mM NaH_2PO_4 pH 8.0, 1 M KCl, 5% (v/v) glycerol and then with 50 mM NaH_2PO_4 pH 8.0, 300 mM NaCl, 5% (v/v) glycerol, 50 mM imidazole. Elution was carried out in 50 mM NaH_2PO_4 pH 8.0, 300 mM NaCl, 5% (v/v) glycerol, 250 mM imidazole. His-tagged Prescission protease was added and the sample was dialyzed overnight in resuspension buffer. The sample was then passed a second time through a His-Trap column, and the flow-through was collected. Finally, a Superdex 75 10/300 chromatographic step was carried out in 20 mM PIPES pH 6.5, 200 mM NaCl.

NPAC dehydrogenase cell pellet was resuspended in 50 mM HEPES pH 7.5, 500 mM NaCl, 40 mM imidazole, 5% (v/v) glycerol, supplemented with 1 mM PMSF. The suspension was lysed by sonication and centrifuged at 70,000 g for 35 min. Cell extract was loaded onto a 5 mL HisTrap column, washed and eluted in 50 mM HEPES pH 7.5, 500 mM NaCl, 250 mM imidazole. The sample step was supplemented with 6xHis-TEV protease and dialyzed overnight, against 2 L of 50 mM HEPES pH 7.5, 500 mM NaCl, 5% (v/v) glycerol. A second His-Trap column was used to remove the His-tag and TEV protease. The flow-through was loaded onto a Superdex 200 16/60 (GE Healthcare) in 50 mM HEPES pH 7.5, 500 mM NaCl, 5% (v/v) glycerol.

NPACΔ205 (linker + dehydrogenase) cell pellet was resuspended in 50 mM HEPES pH 7.5, 5% (v/v) glycerol, 500 mM NaCl, 40 mM imidazole, 1 mM PMSF before cell disruption by sonication and successive centrifugation at 70,000 g for 40 min. The supernatant was loaded onto a HisTrap column and the protein was eluted by adding 250 mM imidazole. Incubation with His-tagged SUMO protease was carried out overnight in dialysis against 50 mM HEPES pH 7.5, 5% (v/v) glycerol, 500 mM NaCl. Both tag and protease were removed through a His-Trap column. The flow through was loaded on a Superdex 200 10/300 in 50 mM HEPES pH 7.5, 5% (v/v) glycerol, 500 mM NaCl, 0.5 mM dithiothreitol.

Enzyme activity assays

Peptides were purchased from ChinaPeptides. Activity measurements were performed with peroxidase-coupled assays on a Clariostar plate reader (BMG Labtech). The reactions were carried out in 50 mM HEPES pH 8.5, 0.1 mM Amplex Red, 0.3 mM horseradish peroxidase, 0.3 μM LSD2Δ30, with and without 3 μM NPAC-linker at different ionic strengths (0 mM NaCl, 100 mM NaCl, 150 mM NaCl, 200 mM NaCl). H3K4me1 and H3K4me2 H3 N-terminal peptides of different lengths (1-21, 1-30, and 1-40), and H3K4me2 K23M K27M 1-40 peptide were serially diluted. Measured fluorescence signal reflects the enzymatic conversion of Amplex Red to resorufin, as described previously (Pilotto et al., 2015). Initial velocity values were fitted to the Michaelis-Menten equation using GraphPad Prism version 6.00 for Windows, GraphPad Software, San Diego California USA, (https://www.graphpad.com/). Inhibition assays were performed at 100 mM NaCl using $H3_{1-40}$ K4me2 substrate and 100 μM putative peptide inhibitor: $H2A_{1-19}$, $H2A_{117-129}$, $H2B_{4-19}$, $H3_{16-40}$, $H3_{21-40}$, $H4_{1-30}$.

Fluorescence polarization

We measured the change in polarization of a TAMRA-labeled 21-bp DNA (5′-AGTCGCCAGGAACCAGTGTCA-3′) through a Clariostar plate reader (BMG Labtech), as previously described (Pilotto et al., 2015). Experiments were carried out in 15 mM Tris pH 8, 0.01% (v/v) Tween 20 with 0-150 mM NaCl and 5 nM DNA. Peptide binding was measured as described (Pilotto et al., 2015).

Analytical size-exclusion chromatography

10 μM (final concentration) semisynthetic NCPs were incubated with 20 μM LSD2Δ30 and 100 μM NPAC-linker (1:2:10 molar ratio) for an hour on ice in 20 mM Tris pH 7.5, 100 mM NaCl. The mixture was loaded onto silica gel columns WTC-030N5 or WTC-030S5 (Wyatt Technology) equilibrated in 15 mM HEPES pH 7.3 (25°C), 200 mM NaCl. The elution profile was recorded at 260, 280, and 400 nm.

LSD2Δ30 was incubated with NPACΔ205 and semisynthetic nucleosomes for one hour in 20 mM Tris pH 7.5, 1 mM EDTA, 1 mM dithiothreitol, 200 mM NaCl. The mixture was loaded onto silica gel columns WTC-030N5 or WTC-030S5 (Wyatt Technology) equilibrated in 15 mM HEPES pH 7.3 (25°C), 200 mM NaCl. The elution profile was recorded at 214, 260, and 280 nm.

Analytical-SEC experiments of NPAC dehydrogenase were performed with Superdex 200 5/150 (Ge Healthcare) on ÄKTAmicro system (Ge Healthcare) in buffer 50 mM HEPES pH 7.5, 100 mM NaCl, 5% (v/v) glycerol. The elution profile was recorded at 214, 260, and 280 nm.

Thermal-shift assays

Thermofluor (Biorad) experiments were carried out in duplicates in 20 μL wells containing 25 μM NPAC dehydrogenase and SYPRO Orange (Invitrogen) 5X in 50 mM HEPES pH 7.5, 500 mM NaCl, 5% (v/v) glycerol without or with 50 μM NADH or NADPH.

HPLC-MS analysis

To avoid contamination by HEPES and reduce salt content, NPAC dehydrogenase protein was first passed through a Hi-Trap Desalting column (GE Healthcare) at 20°C in 200 mM NaCl, 25 mM Tris pH 7.5. Following a published protocol (Lu et al., 2018),

25 μl samples were treated with 115 μl of 40:40:20 acetonitrile:methanol:water and fresh 0.1 M formic acid, followed by addition of 10 μl of 15% (w/v) $NaHCO_3$. The mixture was incubated at −20°C for 20 minutes, and then the sample was centrifuged at 16,000 g for 30 min at 4°C. The supernatant was analyzed by LC-MS. HPLC purification and MS experiments were performed at Centro Grandi Strumenti (University of Pavia, Italy).

Peptide interaction assay (SPOT blot analysis)

Cellulose-bound peptide arrays were prepared using standard Fmoc solid phase peptide synthesis on a MultiPep-RSi-Spotter (INTAVIS, Köln, Germany) according to the SPOT synthesis method provided by the manufacturer, as previously described (Lambert et al., 2019). Human histone peptides (UniProt accession codes: P68431 (histone H3.1), P84243 (histone H3.3) and P62805 (histone H4)) were synthesized on amino-functionalized cellulose membranes (Whatman Chromatography paper Grade 1CHR, GE Healthcare Life Sciences #3001-878) and the presence of SPOTed peptides was confirmed by ultraviolet light (UV, λ = 280 nM). The assay was performed using His_6-tagged recombinant PWWP domain. Protein bound to peptides was detected using horseradish peroxidase-conjugated anti-His antibody (dilution 1:15000, Novagene, # 71841) and the Pierce ECL Western Blotting Substrate (Thermo Fisher Scientific, # 32106). Chemiluminescence was detected with an image reader (Fujifilm LAS-4000 ver.2.0), typically using an incremental exposure time of 2 min for a total of 80 min. Peptide locations on the arrays and their sequences are provided in Table S2.

Isothermal Titration Calorimetry (ITC)

Experiments were carried out on an ITC200 titration microcalorimeter from MicroCal, LLC (GE Healthcare) equipped with a Washing module, with a cell volume of 0.2003 mL and a 40 μl microsyringe. Experiments were carried out at 15°C while stirring at 1000 rpm in ITC buffer (50 mM HEPES pH 7.5 (at 25°C), 150 mM NaCl). The microsyringe was loaded with a solution of $H3.1_{1-40}$ peptide sample (1605.6 μM, in ITC buffer) and was carefully inserted into the calorimetric cell which was filled with an amount of recombinant PWWP protein (0.2 ml, 52.9 μM in ITC buffer). Following baseline equilibration an additional delay of 60 s was applied. All titrations were conducted using an initial control injection of 0.3 μl followed by 38 identical injections of 1 μl with a duration of 2 s per injection and a spacing of 120 s between injections. The titration experiments were designed as to ensure complete saturation of the proteins before the final injection. The heats of dilution were independent of the peptide concentration and corresponded to the heat observed from the last injection, following saturation of ligand binding, thus facilitating the estimation of the baseline of each titration from the last injection. The collected data were corrected for peptide heats of dilution (measured in separate experiments by titrating the peptides into ITC buffer) and deconvoluted using the MicroCal Origin software to yield enthalpies of binding and binding constants as previously described (Filippakopoulos et al., 2012). Thermodynamic parameters were calculated using the basic equation of thermodynamics. In all cases a single binding site model, supplied with the MicroCal Origin software package was employed. Dissociation constants and thermodynamic parameters are listed in Figure S5B.

Biolayer Interferometry (BLI)

Experiments were performed on an Octet RED384 system (FortéBio) at 25°C in 25 mM HEPES, pH 7.5, 100 mM NaCl and 0.5 mM TCEP and 0.01% TWEEN-20 using the FortéBio data acquisition software V.9.0.049. Biotinylated peptides (Alta Biosciences, Histone Set 1-H3 library, F9: $H3_{28-48}$ and G1: $H3_{28-48}$ K36me3) were first immobilized onto Super Streptavidin biosensors (SuperStreptavidin (SSA) Dip and Read Biosensors for kinetic #18-0011, FortéBio), pre-equilibrated in the BLI buffer then quenched in a solution of 5 μM Biotin: baseline equilibration 60 s, peptide loading for 240 s, quenching for 60 s, 1000 x rpm shake speed, at 25°C. The immobilized peptides were subsequently used in association and dissociation measurements performed within a time window of 600 s (base line equilibration 120 s, association for 240 s, dissociation for 240 s, 1000 x rpm shake speed, at 25°C). PWWP concentrations (0.082, 0.24, 0.74, 2.22, 6.66, 20, and 60 μM) were used in order to determine binding constants. Interference patterns from peptide-coated biosensors without protein were used as controls. After referencing corrections, the subtracted binding interference data were analyzed using the FortéBio analysis software (FortéBio data analysis software V.9.0.014) provided with the instrument following the manufacturer's protocols.

SAXS

SEC-SAXS experiments were performed at BM29 beamline of ESRF (Grenoble, France). All samples were analyzed using Nexera High Pressure Liquid Chromatography (HPLC; Shimadzu) system connected online to SAXS sample capillary (Brennich et al., 2017). About 0.2-0.3 mg of sample were injected, at the flow rate of 0.25 mL/min, onto a WTC-030N5 column (Wyatt Technology) pre-equilibrated with 15 mM HEPES pH 7.3, 200 mM NaCl at 20°C. Scattering data were recorded using per sec frame rate on Pilatus 1 M detector located at a fixed distance of 2.87 m from the sample, allowing a global q range of 0.03–4.5 nm with a wavelength of 0.01 nm. Data analysis of collected frames, including blank subtraction and averaging, was carried out using Chromix (Panjkovich and Svergun, 2018). Radii of gyration (Rg), molar mass estimates and distance distribution functions P(r) were computed using both the ATSAS package (Franke et al., 2017; Konarev et al., 2004) and Scatter (Förster et al., 2010), yielding the same values within the experimental errors (Table S3).

Cryo-EM sample preparation and data acquisition

The LSD2/NPAC-linker/semi-synthetic NCP complex was obtained by mixing 20 μM of full-length LSD2 with 10 μM NCP and 100 μM NPAC-linker in 20 mM Tris pH 7.5, 100 mM NaCl. After two-hour incubation on ice, the complex was purified in buffer 20 mM Tris pH 7.5 (4°C), 200 mM KCl in size-exclusion chromatography (Pilotto et al., 2015) (Figure 1D). After purification, the sample was diluted to reach a final concentration of about 3 μM in the presence of 10 μM NPAC-linker in buffer 10 mM KCl, 20 mM Tris pH 7.5 (4°C). Holey carbon grids (Quantifoil copper, 400 mesh, R2/1) were glow-discharged for 5 minutes before use. In a Vitrobot Mark (FEI), 4 μL of sample were placed onto the grid, blotted for 2 s force 1 in 100% humidity at 20°C, and plunged in liquid ethane.

The screening and the first evaluation datasets were collected on a 200 kV microscope (Tecnai Arctica, FEI) equipped with a Falcon II camera (FEI) at the cryo-EM unit of the Nanyang Technological University (Singapore), and on a 300 kV microscope (Polara, FEI) equipped with a K2 Summit (Gatan) at the Grenoble Instruct Center (Grenoble, France). The high-resolution dataset presented in this work was collected on a 300 kV microscope (Titan Krios, FEI/Thermo Scientific) equipped with an energy filter coupled to a K2 Summit (Gatan) at the eBIC of Diamond Light Source (Didcot, UK) with the proposal number em16082. The images were recorded at 130 kX magnification in electron counting mode, pixel size of 1.06 Å, energy filter of 20 e^- and defocus range from 0.7 to 3.05 μm. A total of 2078 40-frames movie stacks were collected with a total dose of 50 e^-A^{-2} in 8 s of exposure time (1.25 e^-A^{-2} per frame).

Image processing

All movie frames were aligned and corrected for beam motion using MotionCor2 in dose-weighting mode (Zheng et al., 2017) and the resulting average micrographs were processed in the framework of RELION 2.1 and 3.0 (Scheres, 2012) as specified. The integrated images were used for CTF estimation with CTFFIND4 (Rohou and Grigorieff, 2015) followed by automated particle picking using a Gaussian blob as reference within the RELION 2.1 workflow. A total of 490,558 particles were extracted from 1906 selected micrographs with a box size of 300 × 300 pixels. The extracted particles were subjected to multiple rounds of 2D classifications and low-population or poorly-defined classes were discarded to remove junk or inconsistent particles. In parallel, an initial ab-initio density map was separately produced by processing the same dataset using cisTEM (Grant et al., 2018). This map was used as a reference, low-pass filtered to 40 Å, for subsequent image processing steps carried out in RELION (Zivanov et al., 2018). The 400,624 particles remaining after 2D classification were subjected to multiple rounds of 3D classifications in RELION 2.1 to yield five distinct classes with resolutions ranging from ~4 – ~8 Å. 3D refinements followed by local resolution filtering were performed using RELION 3.0 (Zivanov et al., 2018) to produce the final maps.

Model building and structure analysis

An initial model for the density map corresponding to the nucleosome core particle (class 1) was generated using a rigid body fit of a crystal structure (PDB: 6ESF) in UCSF Chimera (Pettersen et al., 2004). The fitted model was further improved by manual rebuilding in COOT (Emsley and Cowtan, 2004). For the LSD2-nucleosome complex maps (classes 2 and 3), the crystal structure corresponding to the nucleosome core particle (PDB: 6ESF) was fitted followed by rigid-body docking of the crystal structure of LSD2/NPAC-linker (PDB: 4HSU) into the additional density using UCSF Chimera (Pettersen et al., 2004). Like the nucleosome core particle, the combined models of the LSD2-nucleosome complex were also subjected to manual rebuilding in COOT (Emsley and Cowtan, 2004). The final models were validated using Molprobity (Chen et al., 2010) and EMRinger (Barad et al., 2015).

QUANTIFICATION AND STATISTICAL ANALYSIS

Activity assays

Initial velocity values were fitted to the Michaelis-Menten equation using GraphPad Prism version 6.00 for Windows, GraphPad Software, San Diego California USA, (https://www.graphpad.com/).

Fluorescence polarization

Experiments were carried out in triplicates. K_d values were determined fitting the data to the Hill equation with GraphPad Prism version 6.00 for Windows, GraphPad Software, San Diego California USA, (https://www.graphpad.com/).

Thermal-shift assays

Thermofluor (Biorad) experiments were carried out in triplicates. All data were analyzed using Microsoft Excel.

Domain prediction and sequence alignments

Alignments were performed with Clustal Omega tool of EMBL-EBI web platform (Li et al., 2015), and ESPrit 3 (Robert and Gouet, 2014). Sequence-based predictions were performed with ELM online software (Dinkel et al., 2016). Homologous sequences for both LSD2 and NPAC were retrieved from Uniprot database (Bateman et al., 2017). Twenty representative sequences of GLYR1/NPAC were selected among mammals (*Ailuropoda melanoleuca, Bos taurus, Canis lupus familiaris, Equus caballus, Homo sapiens, Loxodonta africana, Mus musculus, Oryctolagus cuniculus*), amphibians (*Xenopus tropicalis*), reptiles (*Alligator mississippensis, Pelodiscus sinensis*), birds (*Gallus gallus, Taeniopygia guttata*), fishes (*Danio rerio, Takifugu rubripes*), insects

(*Ceratitis capitate, Noplophora glabripennis*), plants (*Anthurium aminicola, Arabidopsis thaliana*), and chromalveolata (*Symbiodinium microadriaticum*).

DATA AND SOFTWARE AVAILABILITY

The cryo-EM maps and atomic coordinates have been deposited in the Electron Microscopy Data Bank and Protein Data Bank under accession codes EMDataResource: EMD-4704 PDB: 6R1T (class 1), EMDataResource: EMD-4705 PDB: 6R1U (class 2), EMDataResource: EMD-4710 PDB: 6R25 (class 3), EMDataResource: EMD-4711 (class 4), and EMDataResource: EMD-4712 (class 5). SEC-SAXS experimental data and ab-initio model have been deposited in Small Angle Scattering Biological Data Bank with accession codes SASBDB: ASDFU3 (LSD2 Δ30 (31-822)), SASBDB: SASDFX3 (nucleosome), SASBDB: SASDFV3 (NPAC dehydrogenase (261-553)), SASBDB: SASDFW3 (NPAC Δ205 (206-553)), SASBDB: SASDFY3 (LSD2 (31-822)/NPAC Δ205 (206-553)/nucleosome).